Island precipitation enhancement and the diurnal cycle in radiative-convective equilibrium

Citation: Cronin, Timothy W., Kerry A. Emanuel, and Peter Molnar. "Island Precipitation Enhancement and the Diurnal Cycle in Radiative-Convective Equilibrium." Q.J.R. Meteorol. Soc. 141, no. 689 (November 7, 2014): 1017–1034.

As Published: http://dx.doi.org/10.1002/qj.2443

Publisher: Wiley Blackwell

Persistent URL: http://hdl.handle.net/1721.1/99153

Version: Author's final manuscript: final author's manuscript post peer review, without publisher's formatting or copy editing

Island Precipitation Enhancement and the Diurnal Cycle in Radiative-Convective Equilibrium

Timothy W. Cronin,[a]* Kerry A. Emanuel,[b] and Peter Molnar[c]

[a] *Department of Earth and Planetary Sciences, Harvard University, Cambridge, Massachusetts, USA*

[b] *Program in Atmospheres, Ocean, and Climate, MIT, Cambridge, Massachusetts, USA*

[c] *Department of Geological Sciences and Cooperative Institute for Research in Environmental Studies (CIRES), University of Colorado, Boulder, Colorado, USA*

*Correspondence to: Timothy W. Cronin, Department of Earth and Planetary Sciences, Harvard University, 20 Oxford Street, Cambridge, MA 02138, USA.

To understand why tropical islands are rainier than nearby ocean areas, we explore how a highly idealized island, which differs from the surrounding ocean only in heat capacity, might respond to the diurnal cycle and influence the tropical climate, especially the spatial distribution of rainfall and the thermal structure of the troposphere. We perform simulations of three-dimensional radiative-convective equilibrium with the System for Atmospheric Modeling (SAM) cloud-system-resolving model, with interactive surface temperature, where a highly idealized, low heat capacity circular island is embedded in a slab-ocean domain. The calculated precipitation rate over the island can be more than double the domain average value, with island rainfall occurring primarily in an intense, regular thunderstorm system that forms in the afternoon to early evening each day. Island size affects the magnitude of simulated island rainfall enhancement, the intensity of the convection, and the timing of the rainfall maximum relative to solar noon. A combination of dynamic and thermodynamic mechanisms leads to a monotonic enhancement of domain-averaged tropospheric temperature with increasing fraction of island surface, which may contribute to localization of ascent over the Maritime Continent and its relationship to the Walker Circulation.

Key Words: Land-Atmosphere Interaction; Deep Convection; Cloud resolving models; Diurnal effects

Received . . .

1. Introduction

Across a range of time scales, ranging from brief and intense convective storms to annual climatology, tropical islands are some of the rainiest places in the world. By examining a high-resolution dataset of satellite observations from the Tropical Rainfall Measurement Mission (TRMM), Sobel *et al.* (2011) found that small islands are typically climatologically rainier than nearby ocean areas; this contrast increases with both island size and island elevation. Land is generally rainier than ocean in the deep tropics; Wang *et al.* (2014) found that in the latitudinal band from 10°S-10°N, rainfall over ocean averages 4.28 mm day^{-1}, while rainfall over land is 12% higher, at 4.79 mm day^{-1}. The land-ocean contrast in rainfall rises in both an absolute and relative sense when considering the islands and shallow seas of the Maritime Continent in the Western Pacific. In a study of rainfall over this region, As-syakur *et al.* (2013) calculated an average rainfall of 5.47 mm day^{-1} over ocean, but a 40% higher average value of 7.62 mm day^{-1} over islands. Though more rain falls on small islands with substantial topography than on small flat islands, rainfall rate and elevation do not correlate for the large islands in the Maritime Continent region (As-syakur *et al.* 2013; Dayem *et al.* 2007).

Because the mean ascent over the Maritime Continent plays a major role in the atmospheric general circulation, it is troubling that the observed land-ocean contrast in mean rainfall is poorly captured by global models. Precipitation biases in the multi-model-mean from the CMIP5 historical experiment show large magnitudes and considerable spatial structure over the Maritime Continent, with low biases over land, especially Borneo, and high biases over the ocean, especially between New Guinea and Sulawesi (see Figure 9.4 in Flato *et al.* 2013). The timing of the observed diurnal cycle of convective rainfall over islands and tropical land (e.g., Yang and Slingo 2001; Biasutti *et al.* 2012) is also generally poorly reproduced by global models (e.g., Liu and Zipser 2008; Guichard *et al.* 2004; Dirmeyer *et al.* 2012; Hohenegger and Stevens 2013). Connecting these disparities has led to hypotheses that the diurnal cycle may be important for the enhancement of time-mean precipitation or convective intensity over islands (Neale and Slingo 2003; Qian 2008; Robinson *et al.* 2008), and that this may also be a missing factor in climate models. The mechanisms responsible for such rectification of the diurnal cycle, however, remain murky, and the hypotheses of different authors are somewhat divergent (throughout this paper, we use the term "rectification" to indicate that the time-mean response of a system to an oscillatory forcing differs from the time-mean response to the time-mean of the forcing).

Neale and Slingo (2003) and Qian (2008) disagree regarding the influence of land-ocean contrasts on rainfall in the Maritime Continent region. Using a General Circulation Model that systematically underestimates precipitation in the region, Neale and Slingo (2003) found that a threefold increase in resolution failed to reduce regional precipitation biases, but that replacing islands with ocean improved the simulation both locally and remotely. In a study of rainfall over Java with a regional climate model (with parameterized convection), Qian (2008) found that a model configuration with realistic topography successfully captured mean rainfall and its diurnal cycle, but that flattening the island or replacing the island with ocean led to unrealistically low rainfall rates. The differing sign of rainfall response to the replacement of land with ocean indicates that island rainfall enhancement mechanisms in Neale and Slingo (2003) and Qian (2008) must also differ. Robinson *et al.* (2008) explored the theoretical idea that the diurnally oscillating sensible heat flux over islands could produce a resonance for islands of a certain spatial scale, thus leading to locally enhanced convective intensity. A common thread in all three of these studies, as well as other work on modeling of precipitation over tropical islands (Sato *et al.* 2009; Robinson *et al.* 2011), is invocation of the importance of dynamical convective forcing due to low-level convergence of land-sea and mountain-valley breezes. The complexity of such circulations in real terrain, however, especially in concert with other differences between the land and ocean lower boundaries, makes it difficult to determine whether or not diurnally varying low-level convergence is essential for rectification. The goal of this paper is to explore rectifying mechanisms due to interaction of the diurnal cycle of insolation and the low heat capacity of an island surface, which can lead to a time-mean precipitation enhancement and ascent over islands.

A related motivation for studying island rainfall, and particularly rainfall over the islands such as those that constitute the Maritime Continent, lies in the potential for linkage between the tectonic and climatic changes of the past several million years. One of the most notable tectonic changes of the past few million years is the steady northward motion of New Guinea and the Australian plate, and the related emergence of many small islands in the Maritime Continent (e.g., Hall 2002). The climate of the early Pliocene may have resembled a "permanent El Niño" state, with higher sea surface temperatures in the East and Central Pacific, warmer global-mean surface air temperatures, and much smaller global ice volume (e.g., Fedorov *et al.* 2006). Dayem *et al.* (2007) compared the correlation between Walker Circulation strength and precipitation in two regions – the Maritime Continent, and the Pacific warm pool. Finding a better correlation of Walker Circulation strength with Maritime Continent precipitation, Dayem *et al.* (2007) hypothesized that reorganization of the Maritime Continent could have "provided a necessary condition for the onset of the Walker Circulation," contributing to a shift out of the "permanent El Niño" regime of the early Pliocene. The extent to which changes in fraction and configuration of islands could have contributed to the large-scale atmospheric circulation changes of the past few million years remains a largely unanswered question.

Extensive study of rainfall over islands has been conducted before, with our understanding of the dynamics of deep convection and rainfall over flat islands greatly improved by the Maritime Continent Thunderstorm Experiment (MCTEX). MCTEX was conducted in late 1995 over the Tiwi Islands of northern Australia, which are relatively flat, and about 150 km long by 50 km wide. MCTEX focused on the remarkable regular convective system known as Hector, which is one of the most intense and predictable mesoscale convective systems in the world; Hector occurred every day during the 2-week intensive observational period from 20 November to 4 December 1995 (Keenan *et al.* 2000). Work on Hector has considered the problem of island rainfall from observational, theoretical, and numerical modeling standpoints, and has considered the importance of many processes, including cumulus merger (Simpson *et al.* 1993), convective triggering by sea breezes (Carbone *et al.* 2000; Crook 2001), aerosol-cloud-precipitation interactions (Connolly *et al.* 2006), and surface the energy budget (Beringer and Tapper 2002). But studies relating to Hector, as well as other geographically nonspecific studies of island convection (Robinson *et al.* 2008, 2011, 2013), have generally shared a focus on weather time scales, where island convection is an initial value problem. We consider climate time scales, where island rainfall becomes a boundary value problem. Thus, we focus on the time-mean effect of an island on the atmospheric thermal structure and distribution of rainfall, rather than on the dynamics of individual mesoscale convective systems.

In this paper, we perform simulations of Radiative-Convective Equilibrium (RCE), where a low-heat capacity island is embedded in a slab-ocean domain. By varying island size, this experimental setup allows us to explore several aspects of island rainfall, including mechanisms for enhancement of time-mean rainfall, differences in convective intensity over land and ocean, and controls on the afternoon timing of the rainfall peak over land. In the context of our simulations, we also explore whether the dynamics of the linear land and sea breeze can be used as tools to understand any of these effects. We describe the details of the design of simulation experiments (Section 2), and present results for a reference-case island and across a range of island sizes (Sections 3.1 and 3.2). We discuss mechanisms for time-mean rainfall enhancement over the island, and find that the troposphere warms with increasing island fraction (Sections 4 and 5). We develop and extend the theory of the linear land and sea breeze, including a comparison of linear and nonlinear terms in the momentum equation for surface winds (Section 6). We examine the diurnal phase relations among solar radiation, surface enthalpy fluxes, surface wind convergence, and precipitation, including simple models for important phase lags (Section 7). Finally, in Section 8, we review our key findings and discuss implications for future work.

2. Methods

We conduct simulations of statistical radiative-convective equilibrium (RCE) using version 6.8.2 of the System for Atmospheric Modeling (SAM, Khairoutdinov and Randall 2003) cloud-system-resolving model. In all of our simulations, the

domain is doubly-periodic, 384 by 384 km in size, and has a stretched grid with 64 vertical levels. We perform simulations with a relatively coarse horizontal resolution of 3 km, with non-rotating dynamics, and no background flow. We use the CAM radiation package, with the mixing ratio of CO_2 fixed at 355 ppm. Microphysics are simulated with the SAM 1-moment parameterization, which has two types of cloud water (cloud water and cloud ice) and three thermodynamically-partitioned hydrometeors (rain, snow, and graupel) (Khairoutdinov and Randall 2003). Subgrid-scale turbulence is simulated with a first-order Smagorinsky closure scheme, and surface fluxes of latent and sensible heat are represented with bulk formulae based on Monin-Obukhov similarity theory. The transfer coefficients for enthalpy fluxes depend on near-surface stability and wind speed, and all parameters used in the surface flux scheme maintain oceanic values even over the island (i.e., there is no land-ocean asymmetry in surface roughness).

We break from the traditional setup of RCE by using interactive surface temperatures everywhere in the domain; the model explicitly solves a prognostic equation for slab surface temperature T_S in each grid cell:

$$C_S \frac{\partial T_S}{\partial t} = Q_S - Q_L - H - E, \tag{1}$$

where Q_S is the net shortwave radiation at the surface (positive downwards), Q_L is the net longwave radiation at the surface (positive upwards), H is the surface sensible heat flux, and E is the surface latent heat flux (with both turbulent fluxes positive upwards). Spatial variation in surface heat capacity, C_S, defines the geometry of the island; for ocean grid cells we set $C_{SO} = 4.2 \times 10^6$ J m^{-2} K^{-1}, corresponding to 1 meter-water-equivalent (m.w.e.), and for land grid cells $C_{SL} = 2.1 \times 10^5$ J m^{-2} K^{-1}, corresponding to 0.05 m.w.e. Our choice of C_{SO} is much smaller than the ∼50 m.w.e. that ought to be used to represent the ocean mixed layer, but use of such a deep slab would result in excessively long equilibration times (Cronin and Emanuel 2013), and 1 m.w.e. is sufficiently large to limit the amplitude of the diurnal cycle of T_S over the ocean to ~ 1 K. The island heat capacity per unit area, C_{SL}, is chosen to match the heat capacity of a layer of soil that interacts with the atmosphere on a diurnal time scale. The heat capacity of this layer is calculated as the product of the volumetric heat capacity of soil, $\sim 2 \times 10^6$ J m^{-3} K^{-1}, and the penetration depth of an oscillating thermal forcing into a uniform diffusive soil, $z(\omega) = \sqrt{2D/\omega} \approx 11$ cm for $\omega = 2\pi$/day and $D = 5 \times 10^{-7}$ m^2 s^{-1} (typical soil properties are taken from Ochsner *et al.* 2001). The water-equivalent depth noted above is roughly half the soil penetration depth scale, because the volumetric heat capacity of soil is roughly half the volumetric heat capacity of water.

Simulation of RCE with interactive surface temperatures and a realistic choice of tropical insolation (e.g., $\overline{I} \sim 420$ W m^{-2}) is likely to result in a runaway greenhouse, since net solar absorption, $(1 - \alpha_P)\overline{I}$, far exceeds the threshold of roughly 310 W m^{-2} for Earth's dry atmospheric composition and surface gravity (see section 4.6 of Pierrehumbert 2010). This problem is rarely broached in the literature, because in the context of tropical meteorology, RCE is usually computed with a fixed surface temperature, and thus the surface implicitly acts as an energy sink that adjusts in magnitude exactly as needed to hold surface temperatures fixed.

There are three broad methods by which we can lower the energy input to the system and avoid thermal runaway. The first is to artificially raise the planetary albedo, α_P; this could be accomplished in SAM by increasing the surface albedo considerably. This option is not as straightforward as it might seem, due to the requirement that one must account for the shortwave opacity of the atmosphere (itself a function of temperature in RCE, and dependent on cloud properties) in calculating the surface albedo required to change the planetary albedo by a specified amount (Donohoe and Battisti 2011). Modification of surface albedo also has the potential to lead to biases in the net energy balance of the atmosphere by increasing shortwave absorption, which could be problematic for large $\overline{I}$.

The second approach, as taken by Romps (2011), is to prescribe a surface energy sink, based on an initial simulation with surface temperatures fixed near desired values. This is likely a better option in general, as it parameterizes the real heat export that occurs in the tropical atmosphere-ocean system, but it makes little sense in our case to prescribe a surface energy sink over land. Furthermore, we have avoided prescribing an energy sink

over only the ocean grid cells because this would introduce a large difference in the time-mean surface energy balance between land and ocean that would predispose the atmosphere to favor convection over land, and it would also lead to a strong dependence of the mean temperature of the domain on island size. In general we have sought to minimize the number of differences between land and ocean grid cells so as to isolate the influence of the diurnal cycle and its interactions with differences in land and ocean heat capacities.

The third approach, which we take, is to reduce the insolation. For calculations of solar zenith angle, we use a latitude of 45° N on the spring equinox (Julian day 80), resulting in a time-mean insolation $\overline{I}$ =310.3 W m^{-2} – about three quarters as large as the time-mean insolation on the equator. Although this approach still has the potential to lead to biases (e.g., in cloud radiative effects, clear-sky radiative heating rates, or the magnitude of surface turbulent fluxes), we think it is the best option of the three that are available. In comparison to the real tropics, reduced insolation in our simulations principally compensates for the lack of heat export by the ocean and atmosphere. With these choices, the sun rises at 6 hours local solar time (LST), top-of atmosphere insolation is maximum at 974.4 W m^{-2} at 12 hours LST, and the sun sets at 18 hours LST.

We perform simulations for 250 days, and the time-mean of output variables such as precipitation indicates an average over the last 125 days of the simulation. The initial condition for all simulations is a sounding with no mean wind, obtained from an earlier long simulation of radiative-convective equilibrium with boundary conditions as noted above and a small square island. The initial surface temperature is set to 296.17 K in all cases. Because simulations are so long, we expect the details of the initial condition to be relatively unimportant. We use islands that are approximately circular to the extent allowed by a Cartesian grid; earlier simulations with a square island (not shown here) suggested that the results we present here are not sensitive to details of island geometry. Our reference-case island has a radius $r_I = 48$ km, occupying less than 5% of the total area of domain.

3. Results

Many of the features of the statistical RCE states we simulate over mixed land-ocean surfaces can be summarized by visualizing the evolution of the cloud and surface air temperature fields over a period of a few days. Here, we briefly describe the phenomenology of the convection in the statistical RCE state, before moving on to discuss some of the results in detail for the reference-case island (Section 3.1), and then across a range of island sizes (Section 3.2).

The island disrupts the background RCE state, of pseudo-random convection over the remote ocean, where clouds of different size and separation scales grow and decay at all times of day. Over the island, clouds and surface air temperature evolve with a distinct, repeating pattern from day to day (see movie of clouds and surface air temperature over a 2-day "intensive observation period" in the Supplemental Materials or at: `http://mit.edu/~twcronin/Public/IPEmovie.mp4`). This pattern is at least superficially consistent with the "cumulus merger" hypothesis of Qian (2008), which ascribes increased island rainfall to merging of individual cumulus cells over the course of the day. Clouds initially form near noon at low levels, around the perimeter of the island, likely in association with the sea breeze. In the early afternoon, these shallow clouds develop into deeper isolated precipitating convective cells. In the late afternoon and early evening, these isolated cells appear to merge together near the center of the island, forming a large, heavily raining, continuously cloudy region of deep convection and strong updrafts. As rainfall over the island peaks in the early evening, downdrafts create a mesoscale cold pool that spreads offshore, abruptly reversing the sea breeze, and propagating as much as 100 km before decaying into the background RCE state of distributed random convection. During the night, there are few clouds over the island, and the boundary layer over the island cools, with a land breeze peaking in strength near dawn. As the sun rises, and the boundary layer over the island is again heated and moistened by turbulent enthalpy fluxes, the cycle repeats. The regular island thunderstorm in our simulations shares many features with real-world convection over flat islands, especially as observed in "Hector" (Keenan *et al.* 2000; Carbone *et al.* 2000).

3.1. *Reference-Case Island*

Regular afternoon convection over the island is associated with a marked change in the time-mean distribution of rainfall across the domain. The simulation with the reference-case island (r_I = 48 km) shows a strong enhancement of the time-mean rainfall rate over the island (6.17 mm day^{-1}), as compared to the time-mean rainfall rate over the ocean (2.94 mm day^{-1}; see Figure 1). Figure 1(b) suggests that the moisture to supply this enhanced rainfall is "stolen" from an annular ocean region just surrounding the island, forming a dry ring with much lower rainfall rates than the domain-average. Along with the enhancement of mean rainfall over the island, there is also mean ascent over the island in the mid-troposphere; the compensating subsidence mostly occurs in the nearby dry ring, but about a quarter of the downward flux of air occurs remotely, in the regions farthest away from the island. In the time-mean over the island, air ascends in the mid-troposphere, but subsides near the surface, where the divergent mesoscale cold pool and land breeze overwhelm the convergent sea breeze. Convection over the island is thus associated with a circulation that has multiple components, with different spatial scales in both the vertical and the horizontal.

Convection over the island is also considerably more intense than convection over the ocean, using high quantiles of surface precipitation rate P, cloud-top height $Z_{\rm top}$, and vertical velocity at 500 hPa w_{500} to define metrics of convective intensity (Table 1). The contrast is particularly sharp at the upper tail of the distributions: the 1-in-10,000 hour ocean precipitation event is nearly matched by the 1-in-1,000 hour island precipitation event, and similar statements hold for cloud-top height and vertical velocities. The values in Table 1 for high quantiles of P, $Z_{\rm top}$, and w_{500} for the ocean have been determined based on the ocean grid cells in the reference-case island simulation, but values from the all-ocean control simulation differ little. The contrast between island and ocean convective intensity in our reference-case island simulation is consistent with the study of Williams (2004); at 7308 km^2, our reference-case island size exceeds the threshold of around 100-1000 km^2 found by Williams (2004) for the observed transition from maritime to continental lightning regimes.

Recurring afternoon convection dominates the timing of precipitation over the island (Figure 2). Nearly all of the precipitation over the island falls in the late afternoon to early evening. The sky over the island is nearly devoid of clouds until noon, and then cloud fraction increases abruptly in the afternoon, peaking just after sunset, roughly an hour after the peak in island-average precipitation rate. Rainfall over the ocean has a weaker diurnal cycle, with a nocturnal peak and a minimum during the late afternoon island convective maximum. Rainfall in the all-ocean simulation also peaks at night, but does not show suppression associated with island convection between 16-20 LST as in the ocean rainfall composite of Figure 2a.

3.2. *Island Size Sensitivity Experiments*

Results for islands of different sizes strongly resemble those for the reference-case island, but the mean rainfall enhancement, convective intensity, and timing of the peak rainfall, all vary considerably with island radius. Here we describe how these three features depend on island size, with more detailed analysis in subsequent sections.

In a long-term average, rain falling on the island must derive from either locally evaporated water, or water vapor converged in the atmospheric column over the island. Local evaporation and atmospheric moisture convergence both contribute ~3 mm day^{-1} to island rainfall, but scale differently with island size (Figure 3). Moisture convergence depends much more strongly on island size than does local evaporation, peaking at around 3.7 mm day^{-1} for a 24-km radius island, and falling to under 2 mm day^{-1} for both the smallest and largest islands. Island evaporation increases from ~2.5 mm day^{-1} for the smallest island to ~3.5 mm day^{-1} for islands above 60 km in radius, with a transition near an island radius of 20 km.

Two metrics of convective intensity – extremes of vertical velocity and surface precipitation rate – both show convection to be more intense over the island than over the ocean, but the two measures do not scale in the same way with island size (Figure 4). The extremes of 500-hPa vertical velocity peak at a relatively small island radius, of ~20 km, but the extremes of precipitation rate peak for almost the largest island. The decline in precipitation rate extremes from r_I=96 km to 120 km may

be related to the finite domain size. Extremes of cloud ice path scale similarly to vertical velocity at 500 hPa, while extremes of cloud water path scale similarly to the surface precipitation rate (data for integrated vertical hydrometeor mass were not saved). Extreme precipitation also appears to increase slightly over the ocean as island size increases; we speculate that this is related to the increasing influence of the island on oceanic storms, but we have not investigated this in detail.

We quantify the timing of the maximum of a variable as the phase of the one-cycle-per-day Fourier component of a diurnal composite of that variable. This represents a more synthetic measure of the timing of a variable such as rainfall, than the alternative of simply selecting the hour of maximum precipitation; this latter choice would be resolution-limited by the frequency of our data output (1/hour), which would give a deceptive staircase appearance for the dependence of timing on island size.

For all island sizes, a chain of lags connects peak insolation to peak precipitation and clouds: surface shortwave radiation peaks just before noon, the surface turbulent fluxes respond by peaking some time later, precipitation follows the surface enthalpy flux maximum, and then cloud fraction follows the precipitation maximum (Figure 5). Surface solar radiation peaks slightly before noon because cloud fraction is greater in the afternoon than in the morning, blocking solar energy from reaching the surface. The phase lag of surface enthalpy fluxes relative to surface shortwave radiation can reach 2-3 hours; this is likely somewhat large compared to the real world. The lag between surface enthalpy fluxes and precipitation increases rapidly with island radius for small islands, then saturates as island size increases further. For the smallest islands, the rainfall maximum occurs in the early afternoon, nearly in phase with peak surface enthalpy fluxes; for the largest islands, the rainfall maximum occurs near sunset, lagging the peak in enthalpy fluxes by nearly four hours. The final lag between rainfall and cloud fraction is on the order of an hour, and increases modestly with increasing island size. This time scale is consistent with a convective life cycle of air-mass showers where heavy rainfall comes from strong updrafts that take on the order of an hour to reach the tropopause and detrain into high anvil clouds (e.g., Emanuel 1994).

4. Mean Rainfall Enhancement

Island rainfall enhancement occurs as a consequence of both island evaporation enhancement relative to the background oceanic evaporation rate, and net atmospheric water vapor convergence over the island. Moisture convergence makes the larger contribution to rainfall enhancement.

Two separate mechanisms govern the enhancement of evaporation over the island and its scaling with radius. The timing of clouds as a function of island size and the consequent varying impact of cloud shading on the surface energy budget largely determine the scaling of evaporation enhancement with island size. As island radius increases, the cloud fraction peak shifts from mid-afternoon to after sunset – possible reasons for this shift are discussed in Section 7. As the cloud fraction shifts later in the day, the contrast in surface cloud radiative effect between island and ocean shifts from negative to positive (Figure 6). By surface cloud radiative effect, we mean the combined shortwave and longwave impact of clouds on net radiation at the surface, calculated by comparing the full radiative transfer calculation to a hypothetical calculation without cloud water or ice.

The evaporation contrast between island and ocean follows the contrast in surface cloud radiative effect, but is shifted upwards by $\sim$10 W m^{-2} (Figure 6); the island evaporates more than the ocean even when cloud radiative effects on surface energy balance over island and ocean are equal. As we show in Appendix A, this systematic offset is a consequence of the nonlinearity of surface cooling processes. A larger variance in surface temperatures implies a shift in the partitioning of surface cooling toward the flux that depends most nonlinearly on surface-air thermal disequilibrium. Because the turbulent exchange coefficient depends on the near-surface stability, and because the Clausius-Clapeyron equation is more nonlinear than the Stefan-Boltzmann equation, increasing the variance of surface temperatures tends to shift the surface energy budget away from radiative cooling and towards evaporative and sensible cooling.

Atmospheric moisture convergence dominates both the time-mean precipitation enhancement and its scaling with radius (Figures 3, 7). We seek physical mechanisms that can rectify an oscillatory forcing into a time-mean circulation, with moisture

convergence and ascent rather than moisture divergence and subsidence. Such mechanisms can be primarily thermodynamic or dynamic, though both thermodynamic and dynamic budgets must balance in either case. An appealing thermodynamic explanation for time-mean ascent over the island would be a surplus in the top-of-atmosphere (TOA) net radiation over the island, in conjunction with some knowledge about the gross moist stability of the circulation (Neelin and Held 1987; Zeng and Neelin 1999; Raymond *et al.* 2009). According to gross moist stability theory, moisture convergence scales with the difference between the net column radiative cooling and net turbulent enthalpy flux from the surface; given surface energy balance, moisture convergence scales simply with the top-of-atmosphere (TOA) net radiation over the island. Neither the time-mean moisture convergence nor the circulation strength, however, appear to scale with the TOA radiative imbalance across the range of island sizes. The TOA net radiation over the island increases with island size, as the time-mean moisture convergence decreases from a peak over relatively small islands (Figure 7). Moreover, TOA net radiation is negative for some of the smallest islands, where time-mean moisture convergence is large (Figure 7). A TOA radiative surplus constitutes neither a necessary nor a sufficient condition for time-mean moisture convergence, though it may still be an important contributor to the time-mean moisture convergence that is being masked by another more important mechanism. Gross moist stability fails as a predictive theory here, because the island-average proportionality factor between moisture convergence and moist static energy divergence is not constant in magnitude or sign with time; even defining the gross moist stability for circulations that vary on time scales that are comparable to lifetimes of convective clouds may be an ill-posed problem. The failure of this thermodynamic mechanism suggests that dynamical mechanisms may be critical to explaining why there is time-mean ascent over the island, especially in some simulations where there is actually a TOA radiative deficit.

One dynamical mechanism that could plausibly rectify the diurnal cycle is related to the nonlinear dependence of convection on stability, and can be distilled into a dry fluid dynamical problem. Consider an infinite half-plane of nonrotating, unstratified fluid, bounded by on the bottom by a rigid wall, with a point on the bottom wall that oscillates in time between buoyancy source and sink, but with no time-mean buoyancy input to the system. The heat source will generate a buoyant plume that will penetrate upward, but the plume will not reverse when heating switches to cooling; rather, a cold pool will form and spread out across the lower boundary (e.g., Killworth and Turner 1982). We expect that although there is no net buoyancy input, there will be a time-mean circulation, which includes deep ascent from the warm convective plume, as well as shallow subsidence from the spreading cold pool. Furthermore, if surface friction acts to limit the strength of the shallow cell enough, there could be time-mean ascent at all heights in the troposphere above the point source of buoyancy.

We can test this convective rectification mechanism in a slightly less idealized setting by using SAM as a dry atmospheric dynamical model with no atmospheric water vapor, clouds, or radiation. We simulate a 2-dimensional atmosphere, with 1 km horizontal resolution and domain length of 1000 km, and 64 vertical levels in a stretched grid. The initial sounding is neutral to dry convection throughout the troposphere, with potential temperature θ=300 K, patched to a T=200 K isothermal stratosphere (the tropopause is just above 10 km); temperatures relax back to this profile everywhere with a 5-day relaxation time scale. To the central 100 km of the lower boundary, but not elsewhere, we apply a sensible heat flux that varies sinusoidally with a period of one day and an amplitude of 0.05 K m s^{-1}, but with zero mean heat input. In terms of anomalous surface buoyancy flux from the spatial-and time mean, this spatially localized oscillating forcing is very similar to results from the more realistic diurnal cycle in full-physics SAM simulations, but rather than acting as a forcing in a totally quiescent background state, islands in full-physics SAM act as a perturbation to statistical radiative-convective equilibrium. In our dry simulation, a circulation indeed develops, with time-mean ascent at all heights over the island and a maximum island-averaged vertical velocity of $\sim$4.5 cm s^{-1} at a height of 4 km above the surface, with divergent flow above and convergent flow below (Figure 8). A shallow circulation develops between the surface and about 1 km, but the near-surface divergence and subsidence associated with it

occur slightly outside the edges of the island, rather than over the island itself.

It is a leap to suppose that this mechanism operates in our full-physics island simulations with SAM, where moisture introduces many additional complexities, including asymmetries between upward and downward motion, alteration of gravity wave dynamics, and the potential for multi-cell circulations with evaporation-driven downdrafts and descent. Furthermore, determining the scaling of the deep circulation with island size and buoyancy forcing amplitude in dry simulations would require much more work than the one case we have shown here. Despite these caveats, the basic rectifying mechanism of convection-stability interaction remains appealing, though it must still be reconciled with the thermodynamic balance of the time-mean circulation. Particularly vexing is the question of how there can be deep time-mean ascent over the island in some simulations where the island atmospheric column is losing energy compared to surrounding columns over the ocean. The answer to this may be simply that the time-mean circulation has many degrees of freedom, and passes through stages during each day where the sign of the Gross Moist Stability reverses; only a small shift in circulation timing or vertical extent might substantially change the time-mean column energetic balance, including the ability to import moist static energy when there is time-mean ascent.

5. Dependence of Mean Temperature on Island Size

Simulations with an island typically have a warmer troposphere and a slightly cooler surface than control simulations with an all-ocean surface. Denoting the island area fraction A_I, we examine the mass-weighted temperature perturbation from a control (all-ocean) simulation as a function of island area fraction (Figure 9). For smaller islands, an increase in A_I of 0.1 corresponds to a mass-weighted atmospheric temperature increase of about 0.8 K. This warming then saturates for the largest island, which occupies nearly a third of the total domain area.

Although the atmospheric column warms with the inclusion of an island, the surface temperature stays nearly the same. The vertical structure of the thermal perturbation in island simulations includes slight cooling at the surface, a strong increase in boundary layer stability, an upward-amplified (roughly moist-adiabatic) temperature increase in the free troposphere, and cooling in the lower stratosphere (Figure 10). The simulation testing the dry convective rectification mechanism also yields a perturbation to the atmospheric thermal structure that is similar to that observed in full-physics simulations with SAM (Figures 10, 11). In particular, the atmosphere is colder at low levels, warmer through most of the depth of the troposphere, and then colder again in the lower stratosphere, compared to the initial sounding. This increase in time-mean static stability due to a localized oscillatory buoyancy source also agrees with results from the laboratory experiments of Griffiths *et al.* (2011).

There are two reasons for the atmospheric warmth of these island simulations, relative to a comparable all-ocean simulation. First, the influence of the island on cloud fraction timing and top-of-atmosphere cloud radiative effect leads to an energetic surplus that warms both the atmosphere and the surface. This warming is especially important for the larger island sizes, where the clouds peak later in the day and there is a consequent strong positive cloud radiative effect and net radiative surplus over the island. Second, as with the simple calculations with an oscillating heat flux to the base of a dry atmosphere (Figure 8), the rectification of greater variability of surface buoyancy fluxes over the island can warm the atmosphere, even where the cloud radiative effect over the island is zero or slightly negative. The subcloud quasiequilibrium theory of moist convection suggests that the free tropospheric temperature profile is strongly linked to the boundary layer moist entropy. But the boundary layer air that supplies a convective cloud reaching the upper troposphere is characterized not by the mean, but by a high quantile, of boundary layer moist entropy. We thus suggest that the temporal variability in the surface turbulent enthalpy flux over the island, which leads to greater variability of boundary layer moist entropy, acts to push the free troposphere towards a warmer moist adiabat. From the perspective of the top-of-atmosphere energy budget, more longwave emission from a slightly warmer atmosphere is balanced by less longwave emission from a slightly cooler surface. We expect that this radiative compensation mechanism, however, would cease to function as water vapor closes off the atmospheric window at temperatures much above those in the current tropics.

As another consequence of variability, time-mean island temperatures within the boundary layer and at the surface itself tend to be lower than one would expect from downward extrapolation of the free-tropospheric thermal profile. The time-mean surface air temperature over the island is reduced due to diurnal variability, a consequence of averaging over a highly stable nocturnal boundary layer and a nearly neutral daytime boundary layer. The cooling becomes even stronger at the surface itself; the mean island surface temperature is cooler than the mean ocean surface temperature by 3.4 to 5.5 K across the range of island sizes. The surprising result that the land surface can be cooler due to the diurnal cycle was previously discussed by Randall et al. (1991), who noted that the global-mean surface temperatures over land in a General Circulation Model simulation with a diurnal cycle of insolation were 2.7 K cooler than in a simulation with diurnal-average insolation. This cooling is largely caused by the nonlinearity of surface energy balance, discussed in Appendix A, which leads to a smaller (or more negative) difference between time-mean surface temperature and time-mean surface air temperature. If the fluxes are sufficiently nonlinear, then surface energy balance can be attained in the time-mean even if the average surface temperature is lower than the average surface air temperature.

The mean ascent over the island can also be thought of as a consequence of the impact of the island on the thermal structure of the atmosphere. In the weak temperature gradient approximation of tropical dynamics, anomalous heating of the free troposphere over a region must be balanced by ascent (e.g., Sobel *et al.* 2001). In attempting to relax upper tropospheric temperatures to a warmer time-mean state, the radiative-convective dynamics over the island can be thought of as a heating that must be balanced by a deep ascending circulation, which in turn converges moisture into the island column. To the extent that the domain-averaged free tropospheric temperature is warmer in simulations with an island, the weak temperature gradient approximation also suggests that larger regions with islands would favor large-scale ascent, with mean subsidence over comparable open ocean regions. The strength of the large-scale circulation that would result, however, is difficult to estimate, and both cloud and ocean dynamical feedbacks could amplify or dampen such a circulation considerably.

6. Relation to Sea Breeze Theory

One major question posed by our results is: what determines the optimal island size for precipitation enhancement? Work by Robinson *et al.* (2008), as well as Rotunno (1983), suggested the importance of an internal length scale, Nz_0/ω, for the response of a shallow linear land/sea breeze circulation to an oscillating heat source with angular frequency ω, scale height z_0, and buoyancy frequency N. Robinson *et al.* (2008) hypothesized a "resonant response" of the linear sea breeze at a certain island size, and their results for convective intensity (see Figure 1 of Robinson *et al.* 2008) bear a strong resemblance to our time-mean atmospheric moisture convergence (Figure 3). Exploration of the theory of the linear sea breeze may thus yield some insight about whether or not sea breeze dynamics play an important role in our results.

The studies by Rotunno (1983) and Robinson *et al.* (2008) both explored the linear sea breeze problem in Cartesian geometry, and largely considered the weakly damped limit. This leaves open questions of the validity of linear theory for fully nonlinear dynamical models (such as SAM), the effects of cylindrical versus Cartesian geometry, and the relevance of the weakly damped limit in a turbulent, dissipative boundary layer. In this section, we analyze the momentum budget of surface winds in our simulations, and show that roughly half of the pressure gradient acceleration is balanced by linear terms. We then develop theory for the linear sea breeze in the case of cylindrical geometry with modest damping, and compute numerical solutions for several example cases. We find that the timing of the linear sea breeze is affected by damping, and that details of the heating function lead to differences in the scaling of sea breeze strength with island size. It is unlikely that the resonant response hypothesis of Robinson *et al.* (2008) explains our scaling of moisture convergence with island size.

6.1. *Decomposition of Surface Wind Momentum Budget*

Previous work by Robinson *et al.* (2008) and Robinson *et al.* (2011) suggested that the internal length scale in linear theory may be useful for understanding the increase in convective intensity

over islands as their size increases. But Robinson *et al.* (2013) noted that the utility of linear theory is somewhat of a puzzle – one might expect real-world sea breezes to behave as nonlinear density currents. Crook (2001) also noted that under weak mean-flow conditions, solving for island-averaged low-level convergence in a weakly stratified boundary layer must account for nonlinear dynamics. We attempt to directly address the basic question of whether the simulated momentum budgets are dominated by linear or nonlinear terms, which ought to serve as the basis for more thorough investigation of one of the two limits. We start by writing the radial momentum equation,

$$\frac{\partial u_r}{\partial t} + u_r \frac{\partial u_r}{\partial r} = -\frac{1}{\rho}\frac{\partial p}{\partial r} - \mathcal{F}_r, \tag{2}$$

where u_r is the radial wind, the left hand size contains linear ($\partial u_r/\partial t$) and nonlinear ($u_r \partial u_r/\partial r$) accelerations, and the right-hand side contains the pressure gradient acceleration ($-(1/\rho)\partial p/\partial r$), as well as a damping term ($\mathcal{F}_r$). Assuming that the pressure gradient acceleration can be thought of as a buoyancy-driven forcing, we can diagnose the linearity of the sea breeze by seeing how much of the spatial structure in a composite of the pressure gradient forcing associated with the sea breeze is explained by linear and nonlinear terms in the surface wind momentum balance:

$$-\frac{1}{\rho}\frac{\partial p}{\partial r} = \overbrace{\frac{\partial u_r}{\partial t} + \alpha u_r}^{\text{Linear Terms}} + \overbrace{u_r \frac{\partial u_r}{\partial r} + \mathcal{F}_{r,\text{nonlin}}}^{\text{Nonlinear Terms}}. \tag{3}$$

Here, we have assumed that the surface drag can be expanded into a linear Rayleigh damping component with rate α, and a nonlinear residual component. For the purpose of understanding the validity of linear theory, we need to quantify the relative magnitudes of the linear and nonlinear terms in (3). We perform this analysis by computing radial and diurnal composites of terms in (3); the linear portion of the damping is assumed to have $\alpha = 3.6 \times 10^{-5}$ s^{-1}, which is estimated based on the surface drag coefficient and thickness of the lowest model level. We diagnose the nonlinear terms as a residual of the pressure gradient acceleration that is unexplained by the linear terms (Figure 12). For the reference-case island simulation, the linear terms account for the majority (58%) of the variance in the pressure gradient acceleration. This finding holds increasingly well for larger island sizes, but the linear terms explain less than half of the spatial variance in the pressure gradient acceleration pattern for smaller island sizes. Also, these conclusions are somewhat sensitive to the choice of α; for the reference-case island simulation, increasing the value of α up to 1×10^{-4} s^{-1} allows up to 77% of the variance to be explained by linear terms. Such a large value of the linear damping coefficient, however, is difficult to motivate physically, so it is likely that this large apparent damping emulates either nonlinear dissipation or momentum advection.

Thus, the momentum budget in our simulations suggests that we may be able to gain some insight about the atmospheric circulation by analyzing the linear sea breeze. Although the nonlinear terms in the radial momentum equation are far from trivial, they do not dominate the budget across the full range of island sizes. Again, some caution is warranted in this conclusion, because the importance of nonlinear terms depends on the value of α, and because boundary layer turbulence is not necessarily well represented by linear damping.

6.2. *Numerical Solutions in Cylindrical Coordinates with Damping*

Several authors have explored the theory of the linear sea breeze, but none to our knowledge have formulated the version of the problem that is most relevant to us, with no Coriolis force, but with cylindrical geometry and modest damping. This last point, regarding the relevance of dissipation, is touched upon by Rotunno (1983), who showed that the linear sea breeze circulation will peak near midnight in an inviscid model, and that significant damping is required to bring the peak circulation back into the afternoon. In a study of the diurnal cycle of temperature and pressure over North America, Li and Smith (2010) also showed that a thermal damping coefficient on the order of $\sim 7 \times 10^{-5}$ s^{-1} is required to match the phase lag of temperature relative to local solar noon. In our simulations, as in the real world, low-level onshore flow peaks in the early to mid afternoon, indicating that damping regulates the phase lag of the simulated sea breeze circulation. Although this damping may be substantially nonlinear in both our simulations and in the real world, in this section we

will follow previous work on the linear sea breeze in assuming linear Rayleigh damping.

We use the Boussinesq equations, driven by a buoyancy forcing function $\mathfrak{B} \equiv Be^{i\omega t}$, which oscillates in time with angular frequency ω. By assuming Rayleigh damping of both momentum and buoyancy with rate α, we can derive an equation for the spatial structure ψ of the overturning streamfunction, for the linear sea breeze (see Appendix B for full derivation):

$$\left(N^2 - \omega^2 + i\omega\alpha\right)\left(\frac{\partial^2\psi}{\partial r^2} + \frac{1}{r}\frac{\partial\psi}{\partial r} - \frac{\psi}{r^2}\right) + \left(\alpha^2 - \omega^2 + 2i\omega\alpha\right)\frac{\partial^2\psi}{\partial z^2} = -\frac{\partial B}{\partial r}. \quad (4)$$

The spatial dependence of the buoyancy forcing, B, was formulated slightly differently by the three studies of Rotunno (1983), Robinson *et al.* (2008), and Robinson *et al.* (2011). One basic insight provided by (4) is that the horizontal gradient of the buoyancy forcing, not the buoyancy forcing itself, acts as the forcing function for the overturning streamfunction. The same amount of spatially integrated buoyancy forcing may produce a different response, and different scaling with island size, if the spatial structure function is an arctangent (Rotunno 1983), a Gaussian (Robinson *et al.* 2008), or a square wave/"top hat" (Robinson *et al.* 2011). For illustrative purposes, we show results for solutions with both an arctangent forcing and a Gaussian forcing, respectively as in Rotunno (1983) and Robinson *et al.* (2008), but with x replaced by r:

$$B_{\text{arctan}} = B_0 e^{-z/z_0}\left\{\frac{1}{2} - \frac{1}{\pi}\arctan\left(\frac{r - r_I}{a_0}\right)\right\} \quad (5)$$

$$B_{\text{Gaussian}} = B_0 e^{-z/z_0} e^{-r^2/r_I^2}. \quad (6)$$

We obtain solutions to (4) by writing the left hand side in discrete form, as the product of a matrix linear operator $\mathbf{L}$ acting on an array of values of ψ. Inverting $\mathbf{L}$ with MATLAB and multiplying by the buoyancy forcing array then yields the streamfunction:

$$\psi = -\mathbf{L}^{-1}\left(\frac{\partial B}{\partial r}\right); \quad (7)$$

the real part of the product $\Psi \equiv \psi e^{i\omega t}$ is the oscillating solution that we seek. For reference conditions of N=0.01 s^{-1}, ω=2π day^{-1}, z_0=250 m, a_0=1000 m, and a buoyancy forcing amplitude corresponding to a sensible heat flux amplitude of H_0=50 W m^{-2} ($B_0 = gH_0/(\rho_0 c_p T_0 z_0) = 5.4 \times 10^{-6}$ m s^{-3}), we calculate the maximum onshore wind speed, and its phase lag from the maximum buoyancy forcing, as a function of island radius, for several different assumptions about the damping rate, forcing function, and geometry (Figure 13). The difference between cylindrical and Cartesian geometry leads to minimal difference in sea breeze strength or timing, but geometric focusing of radial flow in cylindrical geometry leads to a doubling of the convergence of the surface wind, relative to Cartesian geometry. Because the radial gradient of buoyancy forcing is directly tied to the island size in the case of a Gaussian forcing, but has an independent scale (a_0) in the case of an arctangent forcing (see (5) and (6)), the use of a Gaussian forcing leads to weaker maximum radial wind speeds, and a fall-off of wind speed at larger island radii. The arctangent forcing (used in the other four curves) generates a stronger radial wind that approaches a constant for large island sizes.

The impact of the heating function on the sea breeze strength, and particularly its response to changing island size, may explain the different findings of Robinson *et al.* (2008) and Robinson *et al.* (2011). Although Robinson *et al.* (2008) found a clear maximum in metrics of convective intensity for an island half-width of ~20 km, Robinson *et al.* (2011) found little decrease in convective intensity at even much larger islands, either in model simulations or satellite observations of the real world. If the strength of the sea breeze relates to the intensity of subsequent convection, then this difference could be a function solely of the sharpness of the gradient of sensible heat flux at the island edge. Real islands have a sharp (arctangent-like) gradient of sensible heat flux at their edges, rather than a smooth, Gaussian decay, and thus resemble the simulated islands in Robinson *et al.* (2011) more than the simulated islands in Robinson *et al.* (2008).

As noted above, the resonance in Robinson *et al.* (2008) provides an appealing hypothesis for why we find a maximum in moisture convergence for islands of radius ~20 km. Upon closer inspection, however, their theory relates only to the component of surface pressure that is in phase with the heating, and does not incorporate the surface pressure perturbation that is in

quadrature with the heating. This latter component of the pressure perturbation has been referred to as the "thermal continental tide" by Li and Smith (2010), and saturates in the large-island limit (see Appendix C), rather than decaying to zero. Robinson *et al.* (2008) also focus on the strength of the heat low at the center of an island as a measure of convective intensity; however, in the linear limit, it is far from clear that the island-center pressure perturbation (δp) is the best metric for convective intensity. Island-averaged convergence, for instance, might be thought of as a dynamical forcing for convection, and likely scales with $\delta p / r_I^2$, rather than with δp itself. Along these lines, if we estimate the maximum in island-average convergence as $2u_r/r_I$ from the "Reference" curve in Figure 13, we obtain a $\sim r_I^{-1}$ decay at large island sizes (u_r approaches a constant), and a maximum at $r_I = 0$; this matches the large-island fall-off of Robinson *et al.* (2008), but for different reasons, and without an intermediate maximum.

We also cannot rule out the possibility that part of the fall-off with island size in our SAM simulations is limited by the size of the domain; simulations with a smaller domain (not shown) obtain a moisture convergence peak at a slightly smaller island radius. Taken together with the questionable utility of the inviscid limit and the unrealistic spatial smoothness of the heating function in Robinson *et al.* (2008), these findings suggest that the resemblance between Figure 1 of Robinson *et al.* (2008) and our dependence of mean moisture convergence on island size in Figure 3 is likely little more than coincidence.

Linear sea breeze theory may still be useful for explaining some aspects of our simulations. Although it may not determine a resonant scale for mean rainfall enhancement, it closely predicts maximum onshore wind speeds (Figure 14a). In the next section, we also examine whether sea breeze theory may explain the phase lag of precipitation relative to surface enthalpy fluxes, and the scaling of this lag with island size.

7. Phase Lags of Surface Fluxes and Rainfall

It is encouraging that our simulations with SAM often obtain an island precipitation maximum that is lagged by several hours relative to local solar noon, as observed over warm-season and tropical land in the real world, as well as moderate-size islands (e.g., Liu and Zipser 2008; Hamilton 1981; Keenan *et al.* 2000). Convective parameterizations often produce a peak of convective precipitation that occurs in the late morning, or around noon, in sharp contrast to observations (Guichard *et al.* 2004; Dirmeyer *et al.* 2012). It seems likely that resolving the mesoscale dynamics associated with the sea breeze, and resolving the cloud systems themselves, has allowed us to obtain a several-hour lag between local solar noon and peak rainfall. But there are numerous possibilities for what sets this lag, and why in our simulations it is sensitive to island size. Also, our results regarding the lag of the diurnal precipitation peak relative to local solar noon have at least two caveats in comparison to the real world.

The first caveat is that the horizontal resolution in our simulations, at 3 km, is still far too coarse to realistically resolve convection (especially in the boundary layer); we can only really hope to capture convective systems. We must allow for the possibility that coarse resolution makes convection more sluggish in its response to surface heating than it would be in the real world. To address this concern, we have conducted three simulations with island radii of 12, 24, and 48 km, with doubled horizontal resolution of 1.5 km (four times as many grid points). Fortunately, increasing resolution generally has little influence on the timing of precipitation, or its phase lag from the surface enthalpy flux, and leads to a slightly longer lag, rather than a shorter one. For simulations with r_I=48 km, 3-km resolution yields an island rainfall peak at 17:06 LST, and 1.5-km resolution yields a later island rainfall peak at 17:40 LST. Resolution-sensitivity is even weaker for smaller islands; timings of peak surface shortwave radiation, surface enthalpy fluxes, precipitation, and cloud fraction for r_I=12 and 24 km differ by no more than 10 minutes due to doubling resolution. This sensitivity test is far from definitive, as neither resolution we have used will adequately resolve shallow convection or even congestus clouds, but it does suggest that the mechanisms resulting in important phase lags are at least relatively stable to increasing model resolution.

The second caveat concerns the lag of circulation and precipitation relative to the forcing by surface sensible and latent heat fluxes, rather than relative to the solar heating. As noted above with regards to Figure 5, the surface enthalpy fluxes themselves follow local solar noon by as much as 2-3 hours. The common understanding seems to be that surface enthalpy

fluxes peak within an hour of solar noon (e.g., Deardorff 1978; Smith *et al.* 1992; Beringer and Tapper 2002; Betts 2004), though some studies have suggested that the lag could be as large as 2-3 hours (Brubaker and Entekhabi 1995). It is difficult to determine how long the lag between solar forcing and enthalpy fluxes should be. Preliminary examination of gap-filled data from several eddy covariance stations from the AmeriFlux network – which attempt to directly measure surface turbulent fluxes at the landscape scale (data available at `http://cdiac.ornl.gov/ftp/ameriflux/data/`) – suggests that for a range of real land surfaces, the surface enthalpy fluxes lag solar forcing by only ∼10 minutes, much smaller than the 2-3 hours we have simulated.

Below, we present a simple model for why the lag of enthalpy flux relative to solar forcing in our simulations is 2-3 hours, and we show that we can manipulate it by altering the surface heat capacity. Although this lag may be too long compared to the real world, island rainfall is still enhanced, and the upper troposphere is still warmer, in simulations with a lower surface heat capacity and a correspondingly smaller lag. We also hypothesize that the intrinsic spin-up time for a sea breeze circulation partially determines the lag of peak rainfall relative to peak surface enthalpy fluxes in our simulations.

7.1. *Model for enthalpy flux phase lag and sensitivity test*

A linear model of surface energy balance suggests that the relatively long lag of enthalpy fluxes relative to solar forcing in our simulations is due to the combination of relatively weak surface winds, low surface roughness, and the use of a slab model with relatively large heat capacity, rather than a thermally diffusive, multi-layer surface (Deardorff 1978). The lag between peak shortwave radiation at the surface and peak surface turbulent enthalpy fluxes relates directly to the lag of temperature anomaly of a slab surface in response to an oscillating external forcing:

$$C_S \frac{\partial T_S'}{\partial t} = Q_{S0}\cos(\omega t) - \lambda T_S', \tag{8}$$

where Q_{S0} is the oscillating forcing, and λ is a linearization coefficient of the total longwave radiative plus turbulent enthalpy flux loss from the surface, with units of W m^{-2} K^{-1} (see (1)). In response to the oscillatory forcing, the surface enthalpy flux will oscillate, as $\lambda T_S' \sim \cos\{\omega(t-\tau_S)\}$, with a phase lag, τ_S, given by:

$$\tau_S = \frac{1}{\omega}\arctan\left(\frac{\omega C_S}{\lambda}\right). \tag{9}$$

The flux linearization coefficient, λ, is given by the derivative of total energy flux out of the surface with respect to surface temperature, assuming that the temperature of the lowest model level varies much less than the surface temperature itself. Using bulk formulae to express the turbulent enthalpy flux, and assuming the surface emits as a blackbody,

$$\lambda \approx \rho c_K |\mathbf{v}|(c_p + L_v \partial q^*/\partial T) + 4\sigma_B T^3, \tag{10}$$

which varies depending on wind speed, drag coefficient, and absolute temperature. The weak surface winds and low surface roughness in our simulations mean that λ is relatively small. Using the linear coefficient of 14.1 W m^{-2} K^{-1} in the fit from Figure 16 to give an estimate of $\rho c_K|\mathbf{v}|(c_p + L_v\partial q^*/\partial T)$, then inclusion of the Stefan-Boltzmann linearization would give $\lambda \sim$ 20 W m^{-2} K^{-1}. With a surface heat capacity C_{SL} =0.05 m.w.e., this results in an estimated surface enthalpy flux lag of 8970 s, or about 2 hours and 29 minutes. In the set of SAM simulations, the average lag of the turbulent surface enthalpy flux, relative to surface solar radiation, is 8900 s, with a standard deviation of 300 s when considering the range of 11 island sizes. This differs insignificantly from the simple estimate of the linear model, even though Figure 16 shows that surface turbulent enthalpy fluxes are far from linear in their dependence on surface temperature.

The smaller phase lag in observations (perhaps as small as ∼600 s) likely results from both the greater roughness of real land surfaces, and the important role that leaf surfaces play as a functional interface between the atmosphere and surface. Greater surface roughness increases λ, and the dominance of leaf surfaces in the absorption of solar radiation in many vegetation types decreases the effective value of C_S considerably below the value that would be representative of a diffusive soil surface. Taking both of these factors into account, Nobel (2008) estimates the thermal relaxation time scale of a leaf as a mere 18 s.

To test the robustness of some of our results to a more realistic phasing of peak enthalpy fluxes, we perform a set of simulations with a much lower surface heat capacity of 0.005 m.w.e. For $C_{S,L}$=0.005 m.w.e., the linearized surface heat flux theory of (9) predicts a lag of 17 minutes between surface solar radiation and turbulent enthalpy fluxes; the simulated lag between surface solar radiation and turbulent enthalpy fluxes averages a slightly longer ∼25 minutes. In these reduced heat capacity simulations, the lag between peak enthalpy fluxes and precipitation remains on the order of 3 hours, and still increases with island size (Figure 15). The time-mean moisture convergence is weaker, on the order of 1-2 mm day^{-1} (as opposed to 2-4 mm day^{-1} for $C_{S,L}$=0.05 m.w.e.), likely because the TOA radiative surplus over the island is reduced (<0 for all island sizes) as a consequence of a systematically earlier cloud fraction peak. This finding gives further confidence that the time-mean moisture convergence cannot be explained as a result of a top-of atmosphere energy flux surplus and a known Gross Moist Stability. The upper troposphere is also warmer in these simulations than in an all-ocean simulation, but the warming is smaller for a given island size than in Figure 9, and the vertical structure of the warming includes stronger surface cooling than in Figure 10. Despite these differences, our findings of island rainfall enhancement and upper tropospheric warming are qualitatively unaffected by the altered value of island heat capacity.

7.2. *Sea breeze spin-up time scale and precipitation timing*

The phase lag with the strongest dependence on island size is that between peak surface enthalpy flux and peak rainfall and mid-tropospheric ascent (see Figure 5). This lag increases from nearly zero for small islands to ∼3-4 hours for large islands; a plausible mechanism for the lag should also show this scaling with island size. One candidate is the time scale for sea breeze fronts to collide at the center of the island, given by r_I/u_r. Since u_r approaches a constant for large islands, however, this time scale falsely predicts a continued increase for large islands (which would reach ∼11 hours for r_I=120 km and u_r=3 m/s). Linear sea breeze theory offers another mechanism; near-surface convergence responds to the surface heat flux with nearly no delay for small islands, but with a ∼3-4 hours delay for large islands (Figure 13). There are two additional temporal offsets, however, that must be taken into account in order to translate this sea breeze spin-up time scale into a lag between peak surface heat flux and peak precipitation. These two additional offsets may fortuitously cancel.

The first offset results from the delayed relationship between convergence of surface winds and precipitation. We expect precipitation to lag, perhaps another few hours, behind surface convergence, because updrafts would lag surface convergence, and hydrometeors formed in these updrafts do not fall instantaneously. After accounting for this first offset, the linear sea breeze spin-up time scale might then result in a rainfall peak that lags maximum surface heat flux by ∼6 hours in the large island limit – considerably longer than the lag in Figure 5.

The second offset results from the influence of downdrafts on the timing of maximum surface wind convergence. In our simulations, maximum radial wind speeds occur 2-3 hours earlier than predicted by linear sea breeze theory (Figure 14b), and the surface convergence actually leads the surface buoyancy flux for the smallest islands. This offset is likely due to the suppression or reversal of late afternoon convergence by downdrafts and divergence of the surface cold pool once rainfall has begun. Accounting for this second offset would shift the linear sea breeze spin-up time scale to be systematically smaller, and in better agreement with SAM simulation results. Accounting for both the first and second offsets – that the sea breeze peaks earlier than anticipated by dry linear theory, but also that rainfall formation lags surface wind convergence – could allow the linear sea breeze spin-up time to successfully approximate the lag of rainfall relative to peak surface heat fluxes. Given these two compensating moist processes, we refrain from declaring that the spin-up time scale of the dry linear sea breeze fully explains the lag of rainfall relative to peak surface heat fluxes. Nevertheless, we believe that the increase in circulation spin-up time scale with island size is a robust feature of our simulations that is at least qualitatively accounted for by linear theory, and that partially explains the shift in timing of precipitation with island size.

8. Conclusions

We present simulations of radiative-convective equilibrium where a highly idealized, low heat capacity circular island is embedded

in a slab-ocean domain. In all simulations, the presence of an island enhances local rainfall and warms the upper troposphere. Warming of the upper troposphere increases monotonically with the fraction of the domain occupied by islands (Figure 9); local rainfall peaks for islands ∼20 km in radius (Figure 3). Decomposing island rainfall into components from local evaporation and atmospheric moisture convergence reveals that atmospheric moisture convergence dominates the scaling of island rainfall with island size.

We suggest that time-mean moisture convergence is related to a dynamical rectifying mechanism. A spatially localized, oscillatory heat source, with zero time-mean heat input, results in a time-mean circulation in an unstratified, dry atmosphere, because the deep circulation that occurs when the surface is heated is not nullified by the shallow circulation that occurs when the surface is cooled; surface cooling leads to a circulation confined to the lower troposphere (Figure 8). The islands we simulate may act similarly to this idealized oscillating heat source; the heating by islands may perturb the time-mean surface enthalpy flux by only a relatively small amount, but the deep ascent that islands induce during the day is not canceled out by the shallow descent they induce during the night. This mechanism suggests that the diurnal cycle of surface enthalpy fluxes over islands can generate available potential energy for a large-scale circulation with nearby ascent and remote subsidence in the time-mean.

Regarding island evaporation, its scaling with island size and its enhancement relative to the ocean are governed by two separate mechanisms. The timing of clouds becomes progressively later in the day for larger islands (Figure 5), with reduced shortwave reflection by clouds leading to more evaporation as island size increases (Figure 6). A simple model for surface energy balance shows that the larger variance in surface temperatures over the island implies a shift in the partitioning of surface cooling toward evaporative cooling and away from radiative cooling, also resulting in enhancement of island evaporation relative to the ocean.

The presence of an island results in an average warming of the atmospheric column, relative to an all-ocean simulation, and the warming increases monotonically with the fraction of the domain occupied by islands (Figure 9). Warming of the atmosphere is a result of both cloud timing, positive cloud radiative effects on the TOA net radiation over the island, and the increased temporal variability of surface enthalpy fluxes over the island. Increased variability in surface enthalpy fluxes drives the mean thermal profile of the atmosphere towards a warmer state in the upper troposphere, and a cooler state in the boundary layer and at the surface (Figure 10). Mass-weighted atmospheric warming is consistent with the top-of-atmosphere energy budget, because less longwave emission from a slightly cooler surface balances more longwave emission from a slightly warmer atmosphere.

The theory of the linear sea breeze provides a framework for analysis of our results because slightly more than half of the acceleration of surface winds caused by pressure gradient forces is balanced by linear terms in our simulations. Exploration of linear sea breeze theory reveals that the timing of the linear sea breeze is affected by damping, and that details of the heating function lead to differences in the scaling of sea breeze strength with island size. Atmospheric moisture convergence is maximized for islands ∼20 km in radius. Although we offer no alternative theoretical explanation for this peak, we show in Section 6.2 and Appendix C that the peak is unlikely to be explained by the "gravity wave resonance" hypothesis of Robinson *et al.* (2008).

The lag between peak solar forcing and peak surface enthalpy fluxes in most of our simulations is likely longer than is realistic in the real world, but its magnitude can be understood with a linear model of surface energy fluxes. Sensitivity experiments with a very low island heat capacity island reduce this lag, but retain key features of island rainfall enhancement and upper-tropospheric warming described above. Preliminary investigations of the importance of island surface wetness, barotropic mean flow, and removal of cold pools or cloud-radiation interactions, also suggest that local enhancement of rainfall over an island due solely to the interaction of the diurnal cycle and a low-heat capacity surface is a robust result to many parametric assumptions. Sensitivity to mean temperature, island elevation, and vertical wind shear, as well as to microphysics, turbulence, or surface flux parameterizations, however, remain unexplored.

We also hypothesize that the phase lag between surface enthalpy flux forcing and maximum precipitation is set in part by an intrinsic time scale for the spin up of the surface

convergence associated with the linear sea breeze. With regard to this hypothesis, we note that sea breeze-like circulations are not in principle limited to coasts. Heterogeneity of soil moisture over otherwise homogeneous land, for instance, will give rise to a spatially variable amplitude of the surface buoyancy flux, which oscillates with a period of a day. A spectrum of spatial scales of boundary layer circulations would then emerge, mapping to a spectrum of time lags between peak buoyancy flux contrast and peak surface convergence. Our analysis of the linear sea breeze suggests that this mapping could produce a concentration of phase lags near the large-island limiting value, potentially giving rise to a several-hour phase lag between peak buoyancy forcing and peak rainfall even over an all-land surface. This hypothesis could be explored given data about the spatial variability of soil moisture and surface buoyancy fluxes over an otherwise homogeneous land region.

In the real world, island rainfall enhancement may contribute to localization of ascent over the Maritime Continent and its relationship to the Walker Circulation. Together with the weak temperature gradient approximation of large-scale tropical dynamics, the monotonic enhancement of domain-averaged tropospheric temperature with increasing fraction of island surface suggests that regions with islands would favor large-scale ascent, while comparable open ocean regions would favor large-scale subsidence. The strength of such a large-scale circulation is difficult to estimate, and could be amplified or dampened considerably by cloud and ocean feedbacks. If the large-scale circulation is dynamically stable, then we might be expect that the circulation strength scales simply with the anomalous tropospheric warmth and thus with fraction of island area (at least up to some value of island area $\sim 20\%$, as in Figure 9). This study suggests that the sign and magnitude of this thermal anomaly depend on diurnally-forced dynamics on spatial scales of tens of kilometers or less. As General Circulation Models fail to resolve such spatial scales, and simulate the diurnal cycle of convection poorly, they may also fail as a tool for understanding the role of islands in the Walker Circulation.

If the large-scale circulation is dynamically unstable, then heterogeneities in the system, such as islands, could be even more important in determining the location of deep convection and large-scale ascent in the tropical atmosphere. Many theoretical and modeling studies have suggested the possibility that the tropical atmosphere is indeed unstable to large-scale circulation. Nilsson and Emanuel (1999) found spontaneous emergence of a circulation in a two-column model of the tropical atmosphere, with ascent in one column and descent in the other. Raymond (2000) explored the idea that the Hadley circulation could exist as a "Radiative-Convective Instability," which is maintained by feedbacks involving clouds, radiation, water vapor, and convection, rather than by external forcing. Self-aggregation of convection – the phenomenon in modeling studies where convection interacts with larger-scale circulations and organizes into moist regions with ascent and dry regions with descent – is also a manifestation of instability of the tropical atmosphere to large-scale circulation (Bretherton *et al.* 2005; Stephens *et al.* 2008; Craig and Mack 2013; Emanuel *et al.* 2013). If indeed the tropical atmosphere is unstable to large-scale circulation, then even a small island fraction could play a large role in breaking the symmetry of the tropical Pacific. In this manner of thinking, enhanced rainfall, warmer upper tropospheric temperatures, and time-mean ascent over islands might crystallize, nucleate, or spatially phase-lock the large-scale ascending branch of the Walker Circulation.

Acknowledgements

The authors would like to thank Marat Khairoutdinov for freely supplying the SAM model, and Allison Wing for help in using the SAM model. Paul O'Gorman, David McGee, and Adam Schlosser are thanked for useful conversations. This work was funded by NSF Grants AGS 1136466 and 1136480, The Effect of Near-Equatorial Islands on Climate.

Appendix A: Surface energy balance with variance-enhanced fluxes

We develop a simple mathematical model to explain why the increased variance of surface temperatures over land leads to a reduction in the time-mean surface temperature, and shifts the partitioning of surface energy balance away from longwave

radiative cooling, and towards turbulent enthalpy fluxes. Consider second-order expansions of the total turbulent enthalpy flux, $F_K = H + E$, and the net surface longwave cooling, Q_L, where the controlling variable is the thermal disequilibrium, D, between the surface and the atmosphere at the lowest model level:

$$D = T_S - T_1 \tag{11}$$

$$F_K = F_{K0} + b_K D + a_K D^2 \tag{12}$$

$$Q_L = Q_{L0} + b_L D + a_L D^2, \tag{13}$$

where the a's are quadratic coefficients, the b's are linear coefficients, and the F_{K0} and Q_{L0} are the components of the fluxes that do not depend on surface thermal disequilibrium. For the reference-case island, the data are noisy, but the surface enthalpy flux is evidently a nonlinear function of D (Figure 16), with suppression of turbulent fluxes under stable conditions ($D < 0$), and enhancement under unstable conditions ($D > 0$).

Surface energy balance amounts to a requirement that the sum of the time-mean longwave cooling and turbulent enthalpy fluxes equal the time-mean net shortwave heating:

$$0 = \overline{Q_S} - \overline{F_K} - \overline{Q_L}, \tag{14}$$

where $\overline{(\cdot)}$ denotes a time-mean. We decompose the surface thermal disequilibrium into a time-mean and a perturbation:

$$D = \overline{D} + D', \tag{15}$$

and we can then write the time-mean surface energy balance in terms of the mean and the variance of the surface thermal disequilibrium:

$$0 = (\overline{Q_S} - F_{K0} - Q_{L0}) - (b_K + b_L)\overline{D} - (a_K + a_L)\overline{D}^2 - (a_K + a_L)\mathrm{var}(D), \tag{16}$$

where $\mathrm{var}(D) = \overline{(D')^2}$ is the variance of the surface thermal disequilibrium. Now, we can solve for a relationship between the mean thermal disequilibrium ($\overline{D}$) and its variance ($\mathrm{var}(D)$):

$$\overline{D} = \frac{b_K + b_L}{2(a_K + a_L)} \times \left(\left[1 + \frac{4(a_K + a_L)^2}{(b_K + b_L)^2} \left\{ \frac{\overline{Q_S} - F_{K0} - Q_{L0}}{a_K + a_L} - \mathrm{var}(D) \right\} \right]^{1/2} - 1 \right) \tag{17}$$

If both of the quadratic coefficients are positive, then it follows from (17) that increasing variance of the surface thermal disequilibrium must lead to a decrease in the time-mean surface thermal disequilibrium. This was also discussed by Randall et al. (1991), who used an exponential function for surface enthalpy flux, assumed a sinusoidal surface temperature in time, and numerically solved for the decrease in time-mean surface temperature associated with a given amplitude of surface temperature variability.

It is less obvious how an increase in the variance of the surface thermal disequilibrium affects the time-mean partitioning of surface energy balance between longwave cooling and turbulent enthalpy fluxes. Below, we show that increasing variance shifts the balance toward the flux that is more strongly nonlinear; generally speaking this is the turbulent enthalpy flux, as the nonlinearity of the Stefan-Boltzmann equation is small compared to the nonlinearities associated with surface turbulent fluxes of sensible and latent heat. We seek to calculate the sign of the derivative of the mean surface enthalpy flux, $\overline{F_K}$, with respect to the variance of the surface thermal disequilibrium, $\mathrm{var}(D)$. Writing the total derivatives of $\overline{F_K}$ and $\overline{Q_L}$ with respect to $\mathrm{var}(D)$ gives:

$$\frac{d\overline{F_K}}{d\mathrm{var}(D)} = a_K + b_K \frac{d\overline{D}}{d\mathrm{var}(D)} + a_K \frac{d\overline{D}^2}{d\mathrm{var}(D)} \tag{18}$$

$$\frac{d\overline{Q_L}}{d\mathrm{var}(D)} = a_L + b_L \frac{d\overline{D}}{d\mathrm{var}(D)} + a_L \frac{d\overline{D}^2}{d\mathrm{var}(D)}. \tag{19}$$

Because $d\overline{Q_L}/d\mathrm{var}(D) = -d\overline{F_K}/d\mathrm{var}(D)$, we can subtract (19) from (18) after dividing by a_L and a_K to eliminate many terms and obtain:

$$\left(\frac{1}{a_K} + \frac{1}{a_L} \right) \frac{d\overline{F_K}}{d\mathrm{var}(D)} = \frac{d\overline{D}}{d\mathrm{var}(D)} \left(\frac{b_K}{a_K} - \frac{b_L}{a_L} \right). \tag{20}$$

As shown above, $\partial\overline{D}/\partial\mathrm{var}(D)$ is negative – increasing the variance of the surface disequilibrium decreases its time-mean value – and both a's are also positive, so:

$$\mathrm{sgn}\left(\frac{d\overline{F_K}}{d\mathrm{var}(D)}\right) = \mathrm{sgn}\left(\frac{b_L}{a_L} - \frac{b_K}{a_K}\right). \tag{21}$$

If the longwave radiative cooling is more linear than the turbulent surface enthalpy flux, then the turbulent surface enthalpy flux will increase, at the expense of longwave cooling, as the variance of surface temperature increases. The phrase "more linear" here is mathematically specific, in that it refers to a ratio of first-order and second-order coefficients in the expansion of the fluxes about a reference state. For blackbody radiation, and bulk formulae for surface turbulent fluxes with constant exchange coefficient c_K, the ratios of these coefficients are given by:

$$\frac{b_L}{a_L} = \frac{4\sigma T_0^3}{6\sigma T_0^2} = \frac{2}{3}T_0 \tag{22}$$

$$\frac{b_K}{a_K} = \frac{\rho c_K|\mathbf{v}|(L_v dq^*/dT + c_p)}{\frac{1}{2}\rho c_K|\mathbf{v}|L_v d^2q^*/dT^2} \approx (1+B_e)\frac{2RT_0^2}{\epsilon L_v}, \tag{23}$$

where T_0 is a reference temperature, and $B_e = c_p/(L_v dq^*/dT)$ is the equilibrium Bowen ratio, (e.g., Hartmann 1994). For T_0= 290 K, $b_L/a_L \approx 193$, while $b_K/a_K \approx 48$; longwave radiation is more linear than turbulent enthalpy transfer. Based on the fit in Figure 16, $b_K/a_K \approx 26$, smaller than our estimate here from the Clausius-Clayperon nonlinearity alone – the turbulent heat fluxes in the model are made more nonlinear by the dependence of the transfer coefficient c_K on D.

Appendix B: Linear Sea Breeze theory: Equations with Damping

Following Rotunno (1983) and Robinson *et al.* (2008), we start with the Boussinesq equation set, linearized about a resting atmosphere with no horizontal temperature gradients, and with only the continuity equation modified to account for cylindrical geometry:

$$\frac{\partial u}{\partial t} = -\frac{1}{\rho}\frac{\partial p}{\partial r} - \alpha u \tag{24}$$

$$\frac{\partial w}{\partial t} - b = -\frac{1}{\rho}\frac{\partial p}{\partial z} \tag{25}$$

$$\frac{\partial b}{\partial t} + N^2 w = \mathfrak{B} - \alpha b \tag{26}$$

$$0 = \frac{1}{r}\frac{\partial}{\partial r}(ru) + \frac{\partial w}{\partial z}. \tag{27}$$

In (24)-(27), u is the radial wind, p is the pressure perturbation from a background hydrostatic profile, w is the vertical wind, b is the buoyancy, N is the Brunt-Vaisala frequency, α is a Rayleigh damping rate, and $\mathfrak{B} \equiv Be^{i\omega t}$ is a buoyancy forcing function, which is periodic in time and confined in spatial extent to the island. We define a streamfunction $\Psi \equiv \psi e^{i\omega t}$ to satisfy the continuity equation:

$$u = \frac{\partial \Psi}{\partial z} \tag{28}$$

$$w = -\frac{1}{r}\frac{\partial}{\partial r}(r\Psi). \tag{29}$$

Note that for the buoyancy forcing and streamfunction, $\mathfrak{B}$ and Ψ denotes the full functions with time-dependence, while B and ψ denote the spatial structure only. By cross-differentiating and adding the momentum equations to eliminate the pressure gradient terms, and combining the time derivative of the combined momentum equations with the buoyancy equation and its time-derivative, we can obtain an equation for Ψ alone:

$$\left(\frac{\partial^2}{\partial t^2} + \alpha\frac{\partial}{\partial t} + N^2\right)\left(\frac{\partial^2\Psi}{\partial r^2} + \frac{1}{r}\frac{\partial\Psi}{\partial r} - \frac{\Psi}{r^2}\right) + \left(\frac{\partial^2}{\partial t^2} + 2\alpha\frac{\partial}{\partial t} + \alpha^2\right)\frac{\partial^2\Psi}{\partial z^2} = -\frac{\partial\mathfrak{B}}{\partial r}. \tag{30}$$

Because solutions are periodic in time ($\Psi = \psi e^{i\omega t}$), $\partial/\partial t \to i\omega$, and after canceling the factor of $e^{i\omega t}$ from both sides, we obtain:

$$\left(N^2 - \omega^2 + i\omega\alpha\right)\left(\frac{\partial^2\psi}{\partial r^2} + \frac{1}{r}\frac{\partial\psi}{\partial r} - \frac{\psi}{r^2}\right) + \left(\alpha^2 - \omega^2 + 2i\omega\alpha\right)\frac{\partial^2\psi}{\partial z^2} = -\frac{\partial B}{\partial r}. \tag{31}$$

This differs only in the formulation of the Laplacian from the corresponding Cartesian equation:

$$\left(N^2-\omega^2+i\omega\alpha\right)\frac{\partial^2\psi}{\partial x^2}+\left(\alpha^2-\omega^2+2i\omega\alpha\right)\frac{\partial^2\psi}{\partial z^2}=-\frac{\partial B}{\partial x}. \tag{32}$$

In these equations, note that since $N^2 >> \omega^2$, the undamped equations ($\alpha = 0$) are hyperbolic, and the damped equations become elliptic when $\alpha > \omega$, or if the damping time scale is smaller than the time scale of the oscillating buoyancy forcing.

Appendix C: On the resonant response in Robinson *et al.* (2008)

Robinson *et al.* (2008), hereafter RSL08, explore the response of a dry, Boussinesq, weakly damped fluid with uniform stratification, to a buoyancy forcing function that is Gaussian in x, exponentially decaying in z, and sinusoidal in time. They obtain solutions by Fourier transforming the governing equations in space, solving an ordinary differential equation for the vertical structure of the solution as a function of wavenumber, and then analytically evaluating the inverse spatial Fourier transform at $x = z = 0$, to obtain the maximum absolute value of the pressure perturbation at the time when buoyancy forcing is maximum. We extend their results and show that their choice to evaluate the expression for perturbation surface pressure only at the time of maximum heating allows a resonance to appear where one may not really exist.

Modifying terminology for consistency with the rest of this paper [(σ, H, a_0) from RSL08 here become (ω, z_0, r_I)], we take equation (9) of RSL08 as a starting point:

$$\hat{p}(k,z,t)=\frac{\hat{B}(k,z)}{\overline{\omega}\left\{(1/z_0)^2+\gamma^2\right\}}\left(\frac{i}{z_0}e^{z/z_0}-\gamma e^{i\gamma z}\right), \tag{33}$$

where hat symbols denote Fourier transforms, k is the wavenumber in x, z_0 is the scale height of the buoyancy forcing, $\overline{\omega} = \omega - i\alpha$ is the angular frequency of the buoyancy forcing, modified slightly by the small damping parameter α, $\gamma \approx N|k|/\overline{\omega}$ is a vertical wavenumber (the absolute value on k ensures energy propagation is upwards), and $\hat{B}$ is the Fourier transform of the buoyancy forcing:

$$\hat{B}(k,t)=\frac{B_0 r_I}{\sqrt{2\pi}}e^{-k^2r_I^2/4}e^{i(\omega t-\pi/2)}. \tag{34}$$

Taking the inverse Fourier transform of the pressure, we obtain:

$$p(x,z,t)=\mathrm{Re}\left\{\frac{1}{\sqrt{2\pi}}\int_{-\infty}^{\infty}\hat{p}(k,z,t)e^{ikx}dk\right\}. \tag{35}$$

Evaluating the integrand at $x = z = 0$, using above expression for $\hat{p}(k, z, t)$ and dropping the small damping component of $\overline{\omega}$ (so $\overline{\omega} \to \omega$), gives:

$$p(0,0,t)=\frac{B_0 r_I}{2\pi}\int_{-\infty}^{\infty}\mathrm{Re}\left\{e^{i(\omega t-\pi/2)}(i/z_0-N|k|/\omega)\right\}\times \frac{e^{-k^2r_I^2/4}}{\omega\left\{(1/z_0)^2+(Nk/\omega)^2\right\}}dk. \tag{36}$$

RSL08 proceed to further simplify this expression by considering only $t = \pi/(2\omega)$; however, we evaluate the surface pressure at the island center at all times, which affects the solution and its interpretation. To simplify the algebra in (36), we adopt the following nondimensionalizations:

$$\tilde{k}=Nz_0k/\omega \tag{37}$$

$$s=r_I\omega/(2Nz_0). \tag{38}$$

Then, taking the real part of the inverse transform, we obtain:

$$p(0,0,t)=-\frac{B_0z_0}{\pi\omega}\cos(\omega t-\pi/2)\int_{-\infty}^{\infty}\frac{se^{-s^2\tilde{k}^2}}{1+\tilde{k}^2}|\tilde{k}|d\tilde{k} -\frac{B_0z_0}{\pi\omega}\sin(\omega t-\pi/2)\int_{-\infty}^{\infty}\frac{se^{-s^2\tilde{k}^2}}{1+\tilde{k}^2}d\tilde{k}. \tag{39}$$

Both integrands are even functions; we multiply by 2 and transform the bounds of integration to $[0, \infty]$. Also, factoring out e^{s^2} from each integral, we obtain:

$$p(0,0,t)=-\frac{B_0z_0se^{s^2}}{\pi\omega}\cos(\omega t-\pi/2)\int_{0}^{\infty}\frac{e^{-s^2(1+\tilde{k}^2)}}{1+\tilde{k}^2}2\tilde{k}d\tilde{k} -\frac{2B_0z_0se^{s^2}}{\pi\omega}\sin(\omega t-\pi/2)\int_{0}^{\infty}\frac{e^{-s^2(1+\tilde{k}^2)}}{1+\tilde{k}^2}d\tilde{k}. \tag{40}$$

As in RSL08, with a change of variables ($t' = 1 + \tilde{k}^2$), the first integral in (40) is given by the exponential integral $E_1(s^2)$:

$$E_1(s^2) = \int_1^\infty \frac{e^{-s^2 t'}}{t'} dt'. \tag{41}$$

The second integral in (40) is related to Owen's T-function:

$$T(h,a) = \frac{1}{2\pi} \int_0^a \frac{e^{-\frac{h^2}{2}(1+x^2)}}{1+x^2} dx. \tag{42}$$

Owen (1980) (Table 2.4 p. 414), gives an identity for the relevant limit as $a \to \infty$:

$$\begin{aligned} T(h,\infty) &= \frac{1}{2}\left(1 - \frac{1}{\sqrt{2\pi}} \int_{-\infty}^h e^{-\frac{x^2}{2}} dx\right) \\ &= \frac{1}{4}\mathrm{erfc}(h/\sqrt{2}), \end{aligned} \tag{43}$$

where erfc(·) is the complementary error function:

$$\mathrm{erfc}(h) = \frac{2}{\sqrt{\pi}} \int_h^\infty e^{-x^2} dx. \tag{44}$$

Using this information, we find that the second integral in (40) is given by:

$$\int_0^\infty \frac{e^{-s^2(1+\tilde{k}^2)}}{1+\tilde{k}^2} d\tilde{k} = 2\pi T(s\sqrt{2}, \infty) = \frac{\pi}{2}\mathrm{erfc}(s). \tag{45}$$

From this, we finally obtain a closed form for the surface pressure perturbation at the island center:

$$p(0,0,t) = -\frac{B_0 z_0}{\omega} \left\{ f_0(s) \cos(\omega t - \pi/2) + f_1(s) \sin(\omega t - \pi/2) \right\}, \tag{46}$$

where $f_0(s)$ and $f_1(s)$ are functions that scale the pressure perturbation with nondimensional island size, s:

$$f_0(s) = \pi^{-1} s e^{s^2} E_1(s^2) \tag{47}$$

$$f_1(s) = s e^{s^2} \mathrm{erfc}(s). \tag{48}$$

We can also rewrite (46) to make explicit the amplitude and phase of the pressure perturbation:

$$p(0,0,t) = -\frac{B_0 z_0}{\omega} \sqrt{f_0(s)^2 + f_1(s)^2} \times \cos(\omega t - \pi/2 - \phi) \tag{49}$$

$$\phi = \arccos\left(\sqrt{\frac{f_0(s)^2}{f_0(s)^2 + f_1(s)^2}}\right). \tag{50}$$

Figure 17 shows a plot of the two functions f_0 and f_1, as well as the amplitude of the pressure perturbation at the center of the island, $\sqrt{(f_0^2 + f_1^2)}$. Although f_0 has a local maximum for $s = 0.5$, f_1 asymptotically increases towards a value of $1/\sqrt{\pi}$. Furthermore, the amplitude of the overall response has no local maximum as a function of island size. The surface pressure perturbation, evaluated at the time of maximum surface pressure perturbation, does not show evidence of having a resonance. As island size increases, the phase lag of minimum surface pressure relative to maximum heating grows larger, approaching 1/4 cycle, or 6 hours, in the large-island limit.

References

As-syakur A, Tanaka T, Osawa T, Mahendra M. 2013. Indonesian rainfall variability observation using TRMM multi-satellite data. *Int. J. Remote Sens.* 34: 7723–7738. DOI:10.1080/01431161.2013.826837.

Beringer J, Tapper N. 2002. Surface energy exchanges and interactions with thunderstorms during the Maritime Continent Thunderstorm Experiment (MCTEX). *J. Geophys. Res.* 107(D21): 4552. DOI:10.1029/2001JD001431.

Betts A. 2004. The Diurnal Cycle Over Land. In: *Forests at the Land-Atmosphere Interface*, eds Mencuccini M, Grace J, Moncrieff J, McNaughton K. CABI Publishing: Cambridge, pp. 73–93.

Biasutti M, Yuter S, Burleyson C, Sobel A. 2012. Very high resolution rainfall patterns measured by TRMM precipitation radar: seasonal and diurnal cycles. *Climate Dyn.* 39: 239–258. DOI:10.1007/s00382-011-1146-6.

Bretherton C, Blossey P, Khairoutdinov M. 2005. An energy-balance analysis of deep convective self-aggregation above uniform SST. *J. Atmos. Sci.* 62: 4273–4292. DOI:10.1175/JAS3614.1.

Brubaker K, Entekhabi D. 1995. An analytic approach to modeling land-atmosphere interaction 1: Construct and Equilibrium behavior. *Water Resour. Res.* 31: 619–632.

Carbone R, Wilson J, Keenan T, Hacker J. 2000. Tropical Island Convection in the Absence of Significant Topography. Part I: Life Cycle of Diurnally Forced Convection. *Mon. Wea. Rev.* 128: 3459–3480.

Connolly P, Choularton T, Gallagher M, Bower K, Flynn M, Whiteway J. 2006. Cloud-resolving simulations of intense tropical *Hector* thunderstorms: Implications for aerosol-cloud interactions. *Q. J. R. Meteorol. Soc.* 132: 3079–3106. DOI:10.1256/qj.05.86.

Craig G, Mack J. 2013. A coarsening model for self-organization of tropical convection. *J. Geophys. Res.* 118: 8761–8769. DOI:10.1002/jgrd.50674.

Cronin T, Emanuel K. 2013. The climate time scale in the approach to radiative-convective equilibrium. *J. Adv. Model. Earth Syst.* 5: 843–849. DOI:10.1002/jame.20049.

Crook N. 2001. Understanding Hector: The Dynamics of Island Thunderstorms. *Mon. Wea. Rev.* 129: 1550–1563.

Dayem K, Noone D, Molnar P. 2007. Tropical Western Pacific Warm Pool and Maritime Continent Precipitation Rates and Their Contrasting Relationships with the Walker Circulation. *J. Geophys. Res.* 112, D06101. DOI:10.1029/2006JD007870.

Deardorff J. 1978. Efficient Prediction of Ground Surface Temperature and Moisture, with Inclusion of a Layer of Vegetation. *J. Geophys. Res.* 83(C4): 1889–1903.

Dirmeyer P, Cash B, Kinter J, Jung T, Marx L, Satoh M, Stan C, Tomita H, Towers P, Wedi N, Achutavarier D, Adams J, Altshuler E, Huang B, Jin E, Manganello J. 2012. Simulating the diurnal cycle of rainfall in global climate models: resolution versus parameterization. *Climate Dyn.* 39: 399–418. DOI:10.1007/s00382-011-1127-9.

Donohoe A, Battisti D. 2011. Atmospheric and Surface Contributions to Planetary Albedo. *J. Climate* 24: 4402–4418. DOI:10.1175/2011JCLI3946.1.

Emanuel K. 1994. *Atmospheric Convection*. Oxford University Press: New York; 580 pp.

Emanuel K, Wing A, Vincent E. 2013. Radiative-Convective Instability. *J. Adv. Model. Earth Syst.* 5. DOI:10.1002/2013MS000270.

Fedorov A, Dekens P, McCarthy M, Ravelo A, DeMenocal P, Barreiro M, Pacanowski R, Philander S. 2006. The Pliocene Paradox (Mechanisms for a Permanent El Niño). *Science* 312: 1485–1489.

Flato G, Marotzke J, Abiodun B, Braconnot P, Chou S, Collins W, Cox P, Driouech F, Emori S, Eyring V, Forest C, Gleckler P, Guilyardi E, Jakob C, Kattsov V, Reason C, Rummukainen M. 2013. Evaluation of Climate Models. In: *Climate Change 2013: The Physical Science Basis. Contribution of Working Group I to the Fifth Assessment Report of the Intergovernmental Panel on Climate Change* eds Stocker T, Qin D, Plattner G, Tignor M, Allen S, Boschung J, Nauels A, Xia Y, Bex V, Midgley P. Cambridge University Press: Cambridge, United Kingdom and New York, NY, USA.

Griffiths R, Maher N, Hughes G. 2011. Ocean stratification under oscillatory surface buoyancy forcing. *J. Marine Res.* 69: 523–543.

Guichard F, Petch J, Redelsperger J, Bechtold P, Charboreau J, Cheinet S, Grabowski W, Grenier H, Jones C, Kohler M, Piriou J, Tailleux R, Tomasini M. 2004. Modelling the diurnal cycle of deep precipitating convection over land with cloud-resolving models and single-column models. *Q. J. R. Meteorol. Soc.* 130: 3139–3172. DOI:10.1256/qj.03.145.

Hall R. 2002. Cenozoic Geological and Plate Tectonic Evolution of SE Asia and the SW Pacific: Computer-Based Reconstructions, Model and Animations. *J. Asian Earth Sci.* 20: 353–431.

Hamilton K. 1981. A Note on the observed diurnal and semidiurnal rainfall variations. *J. Geophys. Res.* 86(C12): 12122–12126.

Hartmann D. 1994. *Global Physical Climatology*. Academic Press, International Geophysics Series Volume 56: San Diego, 409 pp.

Hohenegger, C., and B. Stevens, 2013: Controls on and impacts of the diurnal cycle of deep convective precipitation. *J. Adv. Model. Earth Syst.* 5: 801–815. DOI:10.1002/2012MS000216.

Keenan T, Rutledge S, Carbone R, Wilson J, Takahashi T, May P, Tapper N, Platt M, Hacker J, Selesky S, Moncrieff M, Saito K, Holland G, Crook A, Gage K. 2000. The Maritime Continent Thunderstorm Experiment (MCTEX): Overview and Some Results. *Bull. Amer. Meteorol. Soc.* 81: 2433–2455.

Khairoutdinov M, Randall D. 2003. Cloud Resolving Modeling of the ARM Summer 1997 IOP: Model Formulation, Results, Uncertainties, and Sensitivities. *J. Atmos. Sci.* 60: 607–625.

Killworth P, Turner J. 1982. Plumes with Time-Varying Buoyancy in a Confined Region. *Geophys. Astrophys. Fluid Dyn.* 20: 265–291.

Li Y, Smith R. 2010. Observation and Theory of the Diurnal Continental Thermal Tide. *J. Atmos. Sci.* 67: 2752–2765. DOI:10.1175/2010JAS3384.1.

Liu C, Zipser E. 2008. Diurnal cycles of precipitation, clouds, and lightning in the tropics from 9 years of TRMM observations. *Geophys. Res. Lett.* 35: L04819. DOI:10.1029/2007GL032437.

Neale R, Slingo J. 2003. The Maritime Continent and Its Role in the Global Climate: A GCM Study. *J. Climate* 16: 834–848.

Neelin J, Held I. 1987. Modeling Tropical Convergence Based on the Moist Static Energy Budget. *Mon. Wea. Rev.* 115: 3–12.

Nilsson J, Emanuel K. 1999. Equilibrium atmospheres of a two-column radiative-convective model. *Q. J. R. Meteorol. Soc.* 125: 2239–2264.

Nobel P. 2008. *Physicochemical and Environmental Plant Physiology, Fourth Edition*. Academic Press: Oxford, UK, 582 pp.

Ochsner T, Horton R, Ren T. 2001. A New Perspective on Soil Thermal Properties. *Soil Sci. Soc. Amer. J.* 65: 1641–1647.

Owen D. 1980. A table of normal integrals. *Communications in Statistics — Simulation and Computation* 9: 389–419.

Pierrehumbert R. 2010. *Principles of Planetary Climate*. Cambridge University Press: Cambridge, UK, 652 pp.

Qian J. 2008. Why Precipitation Is Mostly Concentrated over Islands in the Maritime Continent. *J. Atmos. Sci.* 65: 1428–1441. DOI:10.1175/2007JAS2422.1.

Randall D, Harshvardhan, Dazlich D. 1991. Diurnal Variability of the Hydrologic Cycle in a General Circulation Model. *J. Atmos. Sci.* 48: 40–62.

Raymond D. 2000. The Hadley Circulation as a Radiative-Convective Instability. *J. Atmos. Sci.* 57: 1286–1297.

Raymond D, Sessions S, Sobel A, Fuchs Z. 2009. The Mechanics of Gross Moist Stability. *J. Adv. Model. Earth Syst.*, 1. DOI:10.3894/JAMES.2009.1.9.

Robinson F, Patterson M, Sherwood S. 2013. A Numerical Modeling Study of the Propagation of Idealized Sea-Breeze Density Currents. *J. Atmos. Sci.* 70: 653–667. DOI:10.1175/JAS-D-12-0113.1.

Robinson F, Sherwood S, Gerstle D, Liu C, Kirshbaum D. 2011. Exploring the Land-Ocean Contrast in Convective Vigor Using Islands. *J. Atmos. Sci.* 68: 602–618. DOI:10.1175/2010JAS3558.1.

Robinson F, Sherwood S, Li Y. 2008. Resonant Response of Deep Convection to Surface Hot Spots. *J. Atmos. Sci.* 65: 276–286. DOI:10.1175/2007JAS2398.1.

Romps D. 2011. Response of Tropical Precipitation to Global Warming. *J. Atmos. Sci.* 68: 123–138. DOI:10.1175/2010JAS3542.1.

Rotunno R. 1983. On the Linear Theory of the Land and Sea Breeze. *J. Atmos. Sci.* 40: 1999–2009.

Sato T, Miura H, Satoh M, Takayabu Y, Wang Y. 2009. Diurnal Cycle of Precipitation in the Tropics Simulated in a Global Cloud-Resolving Model. *J. Climate* 22: 4809–4826. DOI:10.1175/2009JCLI2890.1.

Simpson J, Keenan T, Ferrier B, Simpson R, Holland G. 1993. Cumulus mergers in the maritime continent region. *Meteorol. Atmos. Phys.* 51: 73–99.

Smith E, Hsu A, Crosson W, Field R, Fritschen L, Gurney R, Kanemasu E, Kustas W, Nie D, Shuttleworth W, Stewart J, Verma S, Weaver H, Wesely M. 1992. Area-Averaged Surface Fluxes and Their Time-Space Variability Over the FIFE Experimental Domain. *J. Geophys. Res.* 97(D17): 18599–18622.

Sobel A, Burleyson C, Yuter S. 2011. Rain on small tropical islands. *J. Geophys. Res.* 116: 1–15. DOI:10.1029/2010JD014695.

Sobel A, Nilsson J, Polvani L. 2001. The weak temperature gradient approximation and balanced tropical moisture waves. *J. Atmos. Sci.* 58: 3650–3665.

Stephens G, van den Heever S, Pakula L. 2008. Radiative-Convective Feedbacks in Idealized States of Radiative-Convective Equilibrium. *J. Atmos. Sci.* 65: 3899-3916. DOI:10.1175/2008JAS2524.1.

Wang J, Adler R, Huffman G, Bolvin D. 2014. An Updated TRMM Composite Climatology of Tropical Rainfall and Its Validation. *J. Climate* 27: 273–284. DOI:10.1175/JCLI-D-13-00331.1.

Williams E. 2004. Islands as miniature continents: Another look at the land-ocean lightning contrast. *J. Geophys. Res.* 109: 2–6. DOI:10.1029/2003JD003833.

Yang G, Slingo J. 2001. The diurnal cycle in the tropics. *Mon. Wea. Rev.* 129: 784–801.

Zeng N, Neelin J. 1999. A Land-Atmosphere Interaction Theory for the Tropical Deforestation Problem. *J. Climate* 12: 857–872.

Table 1. Convective intensity metrics for reference-case island simulation, as measured by high quantiles of surface precipitation rate P (mm hour^{-1}), cloud-top height $Z_{\rm top}$ (km), and 500-hPa vertical velocity w_{500} (m s^{-1}). Note that although P and w_{500} have continuous distributions, Z_{top} is quantized by the position of model levels. Cloud-top height is defined in SAM as the first model level, marching downwards, where the total overhead cloud ice plus water path exceeds 10 g m^{-2}. All comparisons between land and ocean are significantly different (the two-sample Kolmogorov-Smirnov test rejects the null hypothesis that the land and ocean distributions of P, $Z_{\rm top}$, and w_{500} are the same at the 0.01% significance level).

	P, mm hour^{-1}		$Z_{\rm top}$, km		w_{500}, m s^{-1}	
Quantile	Island	Ocean	Island	Ocean	Island	Ocean
90%	0.078	0.0068	10.5	8.96	0.121	0.098
99%	6.99	3.67	13.0	11.5	0.902	0.369
99.9%	17.9	10.7	14.0	13.0	2.66	1.59
99.99%	30.4	18.0	15.0	13.5	4.17	2.86

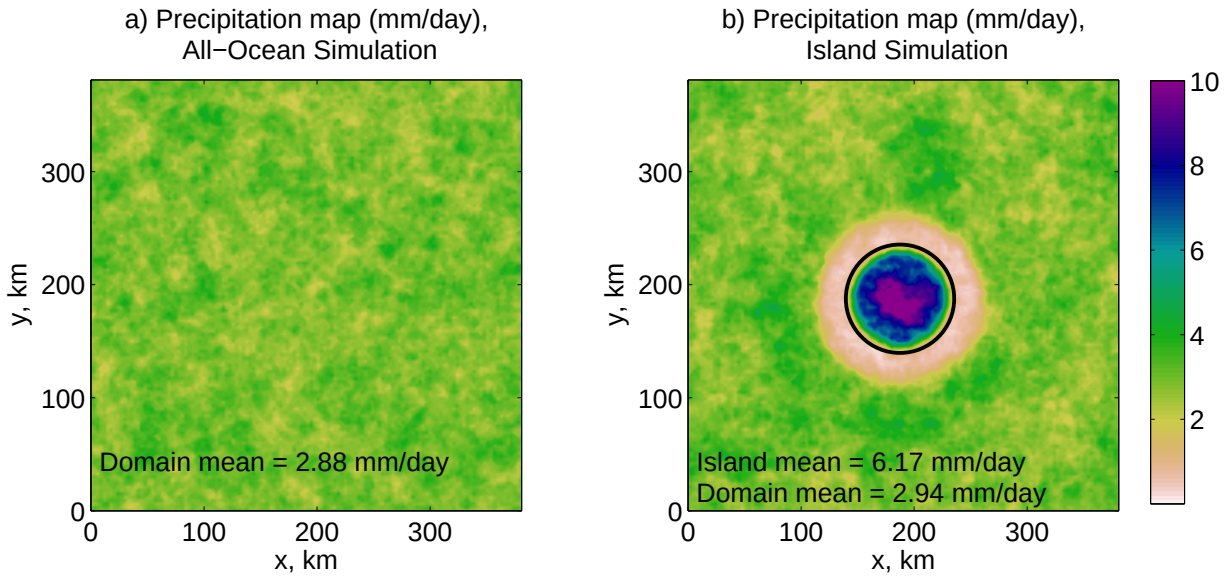

Figure 1. Map of time-mean precipitation rate at the surface for a) control simulation with a homogeneous slab-ocean surface, and b) the reference-case island simulation with r_I =48 km (the spatial extent of the island is denoted by the black circle on subfigure b)). Text on a) indicates the time-and spatial-mean precipitation rate for all grid cells; corresponding text on b) also includes the time-and spatial-mean precipitation rate for island grid cells only.

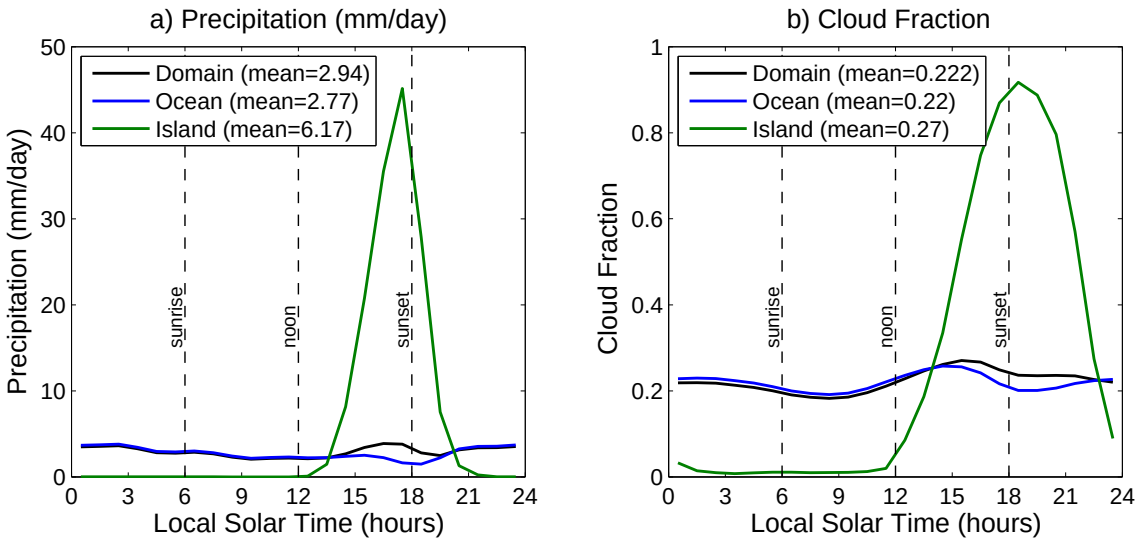

Figure 2. Diurnal composites of a) average precipitation rate (mm day^{-1}), and b) average fraction of grid cells that are cloudy. Composites are calculated for each hour of the day for island grid cells (green), ocean grid cells (blue), and all grid cells (black), for the reference-case island simulation with r_I =48 km, and represent averages over the last 125 days of the simulation. Dashed vertical lines indicate timing of sunrise, sunset, and local solar noon.

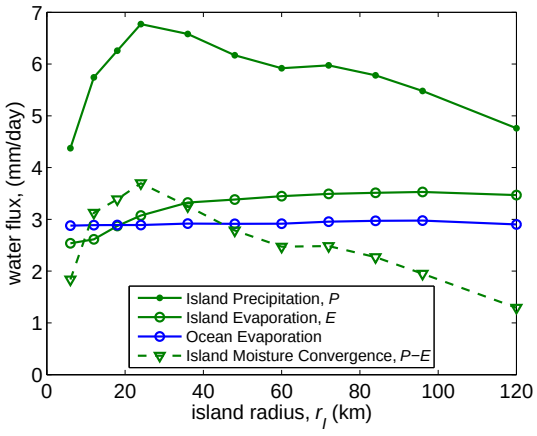

Figure 3. Plot of island precipitation P (green dots), island evaporation, E (green circles), atmospheric moisture convergence over the island, $P - E$ (green triangles), and ocean evaporation rate (blue circles), in mm day^{-1}, against island radius, r_I. Evaporation from the island surface is larger than evaporation from the surrounding ocean for all but the smallest islands.

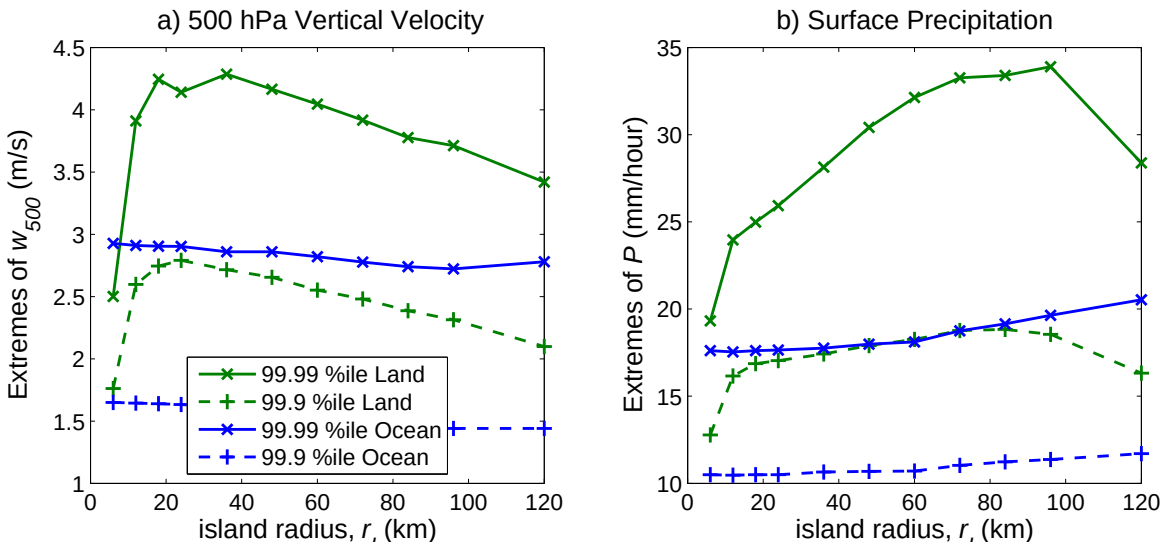

Figure 4. Plot of two measures of convective intensity against island radius: extremes of a) w_{500}, m s^{-1}, and of b) surface precipitation rate, mm hour^{-1}. The 99.99% (solid lines) and 99.9% (dashed lines) quantiles over both island (green) and ocean (blue) are plotted; convection over the island is considerably more intense by both vertical velocity and precipitation rate metrics, but the two do not show the same scaling with island size.

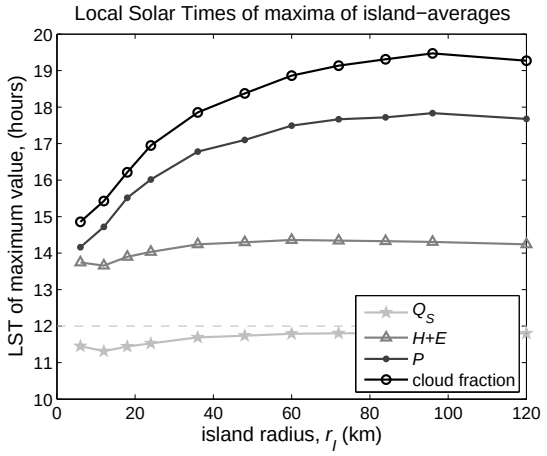

Figure 5. Plot of phases of the maxima of island-averaged surface solar radiation Q_S (stars), surface enthalpy fluxes $H + E$ (triangles), precipitation P (dots), and cloud fraction (open circles) against island radius, for a set of simulations with SAM. The phase of the maxima of all four variables is calculated from the 1/day Fourier component of each variable, averaged over all island grid cells.

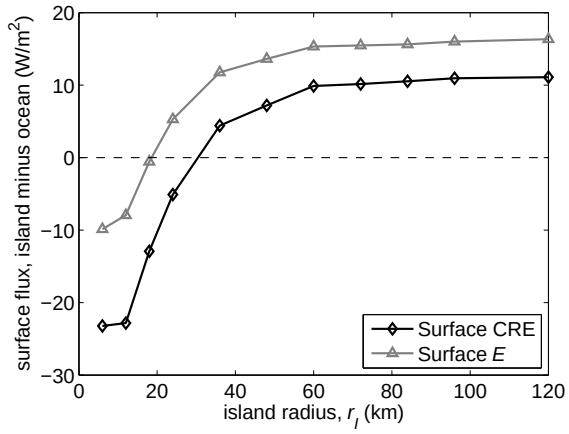

Figure 6. Plot of island minus ocean contrasts in surface cloud radiative effect CRE (diamonds) and evaporation E (triangles), as a function of island radius. The contrast between island and ocean evaporation rates follows the island-ocean cloud radiative effect contrast, but is further increased by nonlinearities in the surface energy budget (see Appendix A). The surface cloud radiative effect is defined as the combined shortwave and longwave impact of clouds on net radiation at the surface, calculated by comparing the full radiative transfer calculation to a hypothetical calculation without cloud water or ice.

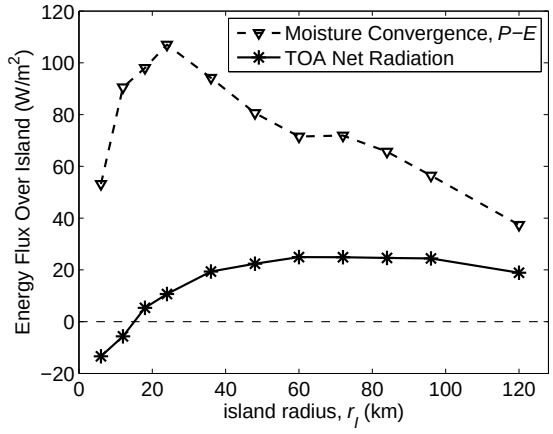

Figure 7. Plot of the island-averaged atmospheric latent heat convergence $P - E$ (triangles), and island-averaged top-of-atmosphere (TOA) net radiation (asterisks) against island radius, for a set of simulations with SAM. There is little correlation between TOA net radiation and moisture convergence, across the set of island sizes.

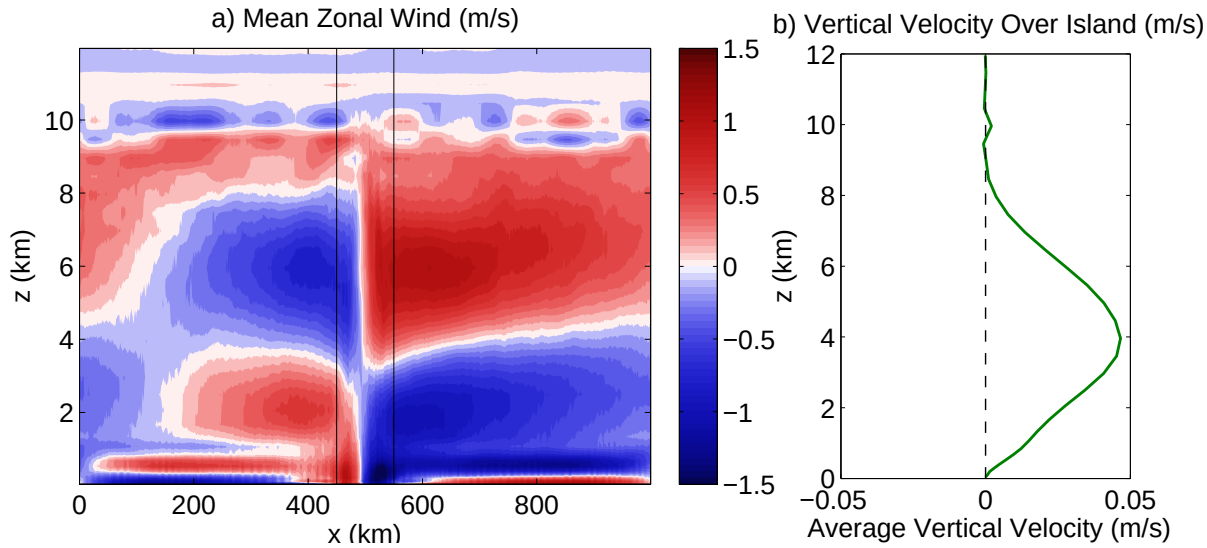

Figure 8. Plot of mean circulation in 2D dry simulation with SAM; subplots show a) mean zonal wind and b) mean vertical velocity from x=450 to x=550 km. As described in the text, a zero-mean sinusoidal buoyancy forcing is applied to the lowest model level, for the region between vertical black lines in a).

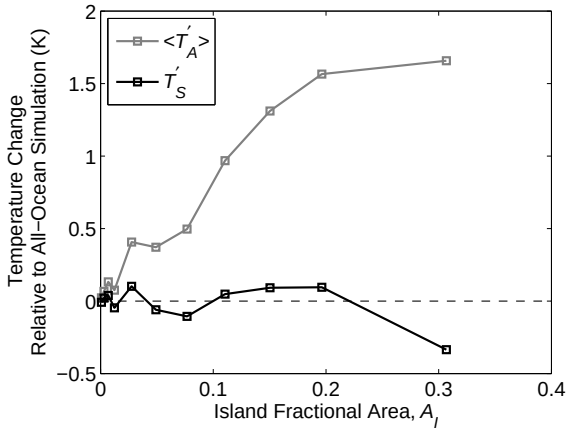

Figure 9. Plot of the mass-weighted atmospheric temperature perturbation ($\langle T_A' \rangle$, gray), and the surface temperature perturbation (T_S', black) against island area fraction A_I. Both variables are averaged over the whole domain, and the perturbation is considered relative to comparable means from an all-ocean simulation.

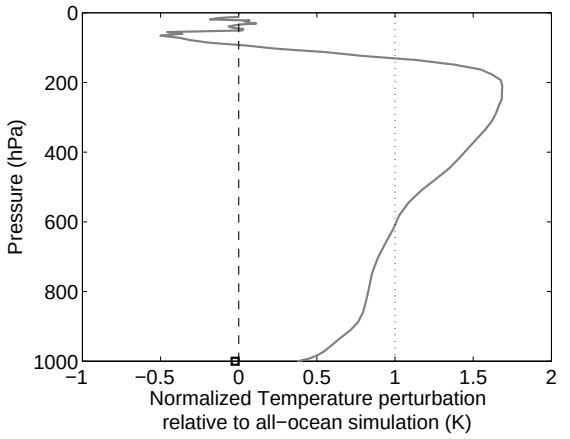

Figure 10. Plot of the normalized vertical structure of domain-average temperature perturbation averaged over the simulations shown in Figure 9. The gray solid line showing the vertical structure of warming is normalized to have a mass-weighted average of 1 K, and the average surface temperature decrease is shown with the black square.

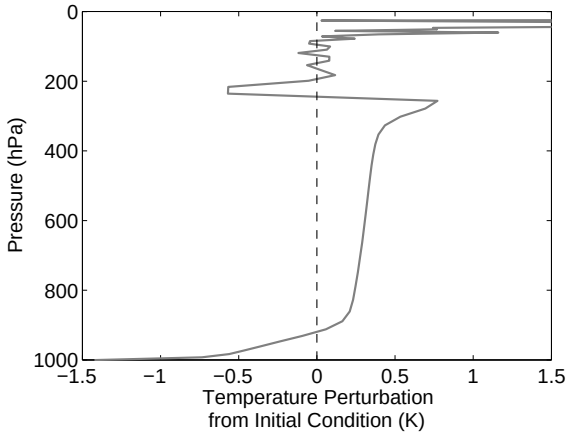

Figure 11. Plot of vertical structure of domain-average temperature perturbation from the initial condition in the 2D dry simulation with SAM (circulation shown in Figure 8).

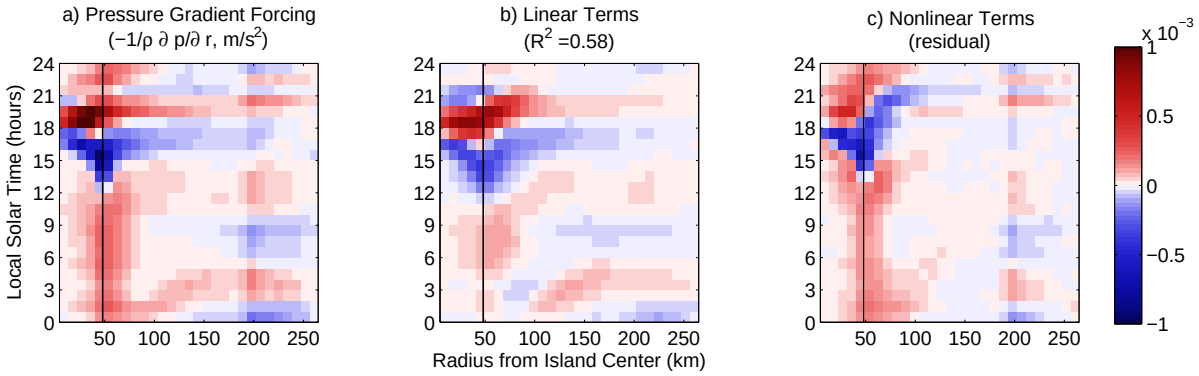

Figure 12. Radially and diurnally composited plot of the terms in the radial momentum budget for surface winds, in the reference-case island simulation (radius:left-to-right, local solar time: bottom-to-top). Subplots show a) Pressure gradient acceleration (m s^{-2}), b) linear terms in surface wind radial momentum equation ($\partial u_r/\partial t + \alpha u_r$) and c) the inferred sum of nonlinear terms in the radial momentum equation; see (3). The majority (58%) of the variance in the pressure gradient acceleration is explained by the sum of the linear terms.

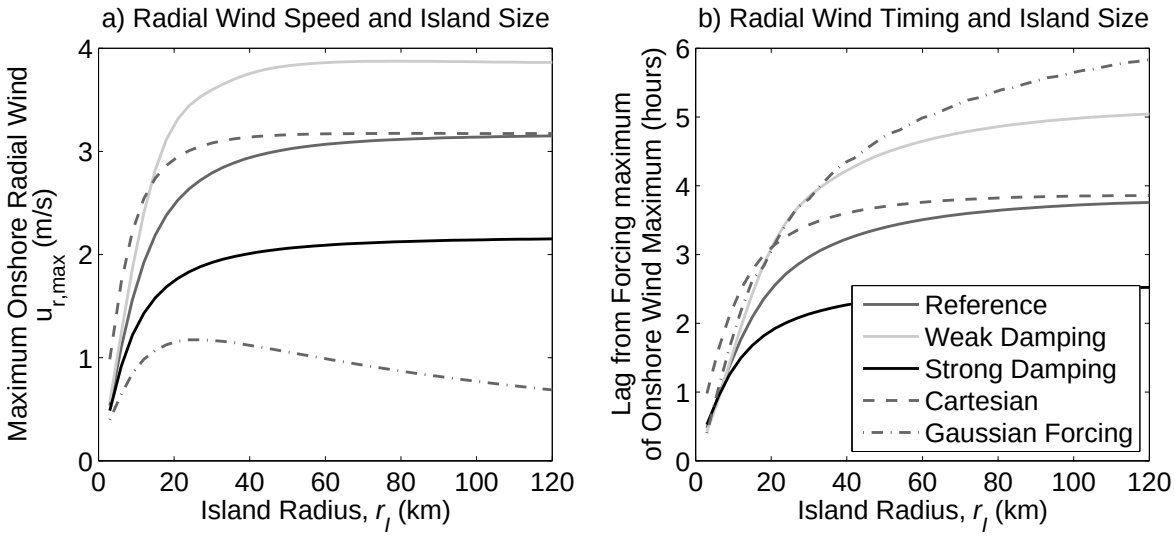

Figure 13. Plots of a) maximum onshore wind speed (m s^{-1}) and b) lag between peak buoyancy forcing and maximum onshore wind, against island radius, from numerical solutions to the linear sea breeze equations (4). The "Reference" case uses polar coordinates, and α=5×10^{-5} s^{-1}; "Weak Damping" (lighter gray) and "Strong Damping" (black) solutions use α=2×10^{-5} s^{-1} and α=1×10^{-4} s^{-1}, respectively. The "Cartesian" case (dashed line) differs from the "Reference" case only in geometry. The "Gaussian" case (dash-dotted line) uses a Gaussian buoyancy forcing, as in (6); the other four cases all use an arctangent forcing (5).

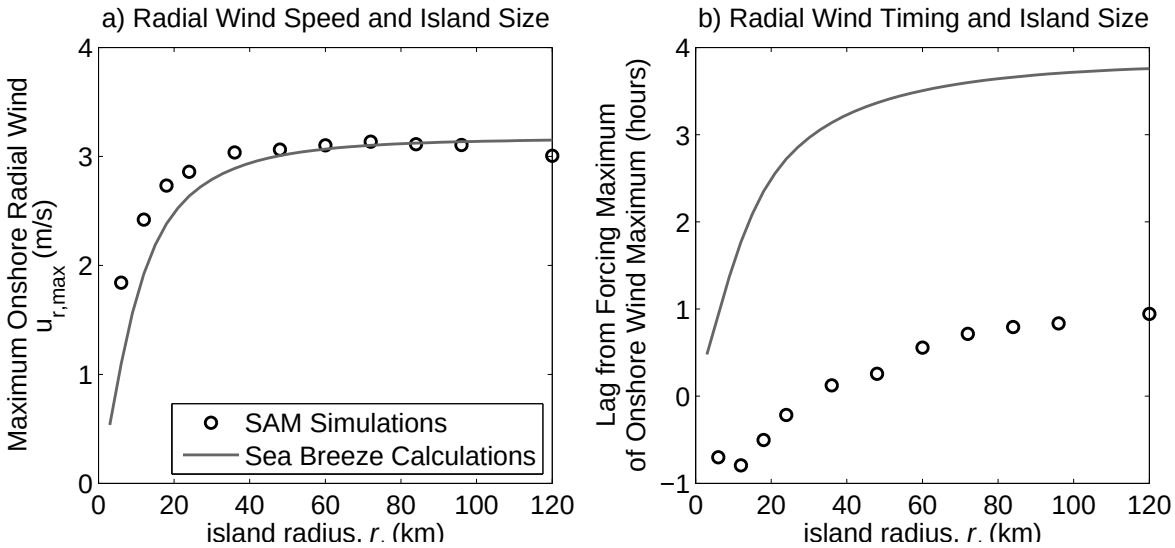

Figure 14. As in Figure 13, but including results from SAM; plots of a) maximum onshore wind speed (m s^{-1}) and b) lag between peak buoyancy forcing and maximum onshore wind, against island radius, for both SAM simulations and linear sea breeze theory. The amplitude of the surface buoyancy forcing in the linear sea breeze theory is taken to roughly match that from SAM.

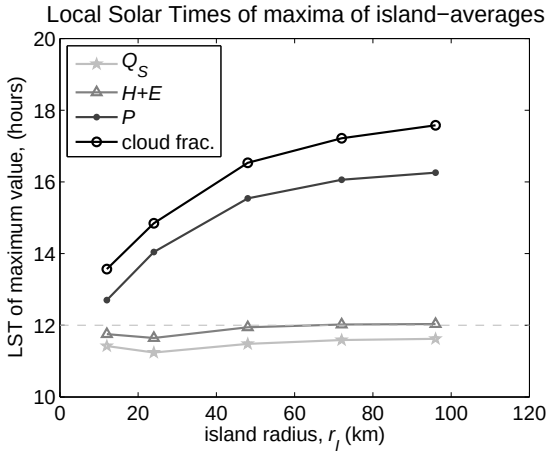

Figure 15. As in Figure 5; plot of phases of the maxima of island-averaged surface solar radiation Q_S (stars), surface enthalpy fluxes $H + E$ (triangles), precipitation P (dots), and cloud fraction (open circles) against island radius, for a set of simulations with SAM with a reduced island surface heat capacity.

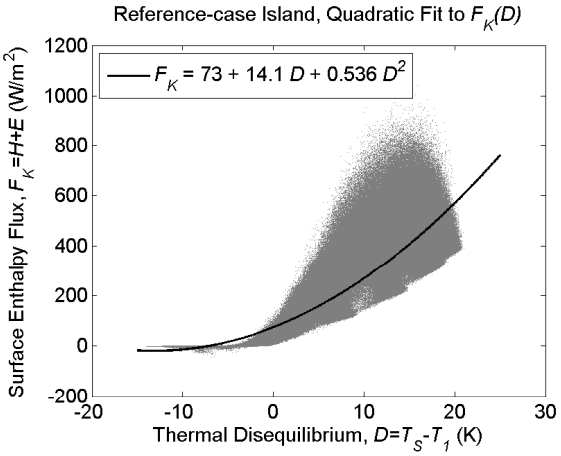

Figure 16. Plot of turbulent enthalpy flux (gray points), F_K, as a function of the thermal disequilibrium between the surface and lowest model level temperature, $D = T_S - T_1$, and a fit to these data (black line) (see Appendix A). The fit is shown for the reference-case island, based on 125 days of hourly-averaged data over all land grid points.

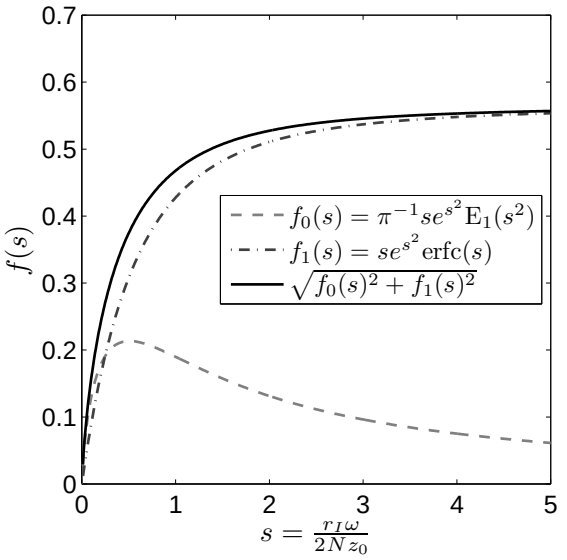

Figure 17. Plot of scaling functions $f_0(s)$ (dashed line) and $f_1(s)$ (dash-dotted line) for the strength of the surface pressure response to a spatially Gaussian and temporally oscillating heating function, for linear, dry, Boussinesq sea breeze theory (See Appendix C). The function $f_0(s)$ is essentially the same as that shown in Figure 1 of Robinson *et al.* (2008), except that it is not multiplied by the pressure drop scale factor, $-B_0 H/\sigma$. The solid black curve shows the magnitude of $f_0(s)$ and $f_1(s)$ when they are added in quadrature, as they are in the time-dependent solution for the minimum surface pressure.

